EQMARL: ENTANGLED QUANTUM MULTI-AGENT REINFORCEMENT LEARNING FOR DISTRIBUTED COOPERATION OVER QUANTUM CHANNELS

Anonymous authors
Paper under double-blind review

ABSTRACT

Collaboration is a key challenge in distributed multi-agent reinforcement learning (MARL) environments. Learning frameworks for these decentralized systems must weigh the benefits of explicit player coordination against the communication overhead and computational cost of sharing local observations and environmental data. Quantum computing has sparked a potential synergy between quantum entanglement and cooperation in multi-agent environments, which could enable more efficient distributed collaboration with minimal information sharing. This relationship is largely unexplored, however, as current state-of-the-art quantum MARL (QMARL) implementations rely on classical information sharing rather than entanglement over a quantum channel as a coordination medium. In contrast, in this paper, a novel framework dubbed entangled QMARL (eQMARL) is proposed. The proposed eQMARL is a distributed actor-critic framework that facilitates cooperation over a quantum channel and eliminates local observation sharing via a quantum entangled split critic. Introducing a quantum critic uniquely spread across the agents allows coupling of local observation encoders through entangled input qubits over a quantum channel, which requires no explicit sharing of local observations and reduces classical communication overhead. Further, agent policies are tuned through joint observation-value function estimation via joint quantum measurements, thereby reducing the centralized computational burden. Experimental results show that eQMARL with Ψ^+ entanglement converges to a cooperative strategy up to 17.8% faster and with a higher overall score compared to split classical and fully centralized classical and quantum baselines. The results also show that eQMARL achieves this performance with a constant factor of 25-times fewer centralized parameters compared to the split classical baseline.

1 INTRODUCTION

Quantum reinforcement learning (QRL) is emerging as a relatively new class of quantum machine learning (QML) for decision making. Exploiting the performance and data encoding enhancements of quantum computing, QRL has many promising applications across diverse areas such as finance (Herman et al., 2022), healthcare (Flöther, 2023), and even wireless networks (Narottama et al., 2023). Its multi-agent variant, quantum multi-agent reinforcement learning (QMARL), is of specific interest because of the potential synergies between decentralized agent cooperation and quantum entanglement. Indeed, in quantum mechanics (Einstein et al., 1971), entanglement is a distinctly quantum property that intrinsically links the behavior of one particle with another regardless of their physical proximity. The use of entanglement in the broader field of QML is a recent notion. Few core works like Mitarai et al. (2018) and Du et al. (2020) use entangled layers within variational quantum circuit (VQC) designs to link the behavior of *quantum bits* (or *qubits*) within a single hybrid quantum model. Even in the recently proposed quantum split learning (QSL) framework (Yun et al., 2023a), entanglement is only used locally within each VQC branch of the quantum split neural network (QSNN) model. What has not yet been explored, however, is using entanglement to *couple* the behavior of multiple QML models. In QMARL, the use of entanglement can be further extended to the implicit coordination amongst agents during training time. Historically, in both purely classical and quantum multi-agent reinforcement learning (MARL), classical communication, shared replay buffers, centralized global networks, and fully-observable environment assumptions have all

proven to be viable methods for coordinating a group policy (Yun et al., 2022a; 2023b; 2022b; Chen, 2023; Park et al., 2023; Kölle et al., 2024). Even QSL, which is not exclusive to MARL, relies fully on classical communication between branches of the QSNN (Yun et al., 2023a). None of these approaches, however, take advantage of the available quantum channel and quantum entanglement as coupling mediums across decentralized agents or model branches, and opt instead for more classical methods of coordination. In short, entanglement is one such phenomenon of quantum mechanics that has not yet been fully explored in the context of cooperation in QMARL settings.

In contrast to prior art, we propose a novel framework dubbed *entangled QMARL (eQMARL)*. The proposed eQMARL is a distributed actor-critic framework, intersecting canonical centralized training with decentralized execution (CTDE) and fully decentralized learning, that facilitates collaboration over a quantum channel using a quantum entangled split critic. Our design uniquely allows agents to coordinate their policies by, for the first time, splitting the quantum critic architecture over a quantum channel and coupling their localized observation encoders using entangled input qubits. This uniquely allows agents to cooperate over a quantum channel, which eliminates the need for observation sharing amongst the agents, and further reduces their classical communication overhead. Also, agent policies are tuned via joint observation-value function estimation using joint quantum measurements across all qubits in the system, which minimizes the computational burden of a central server. As will be evident from our analysis, eQMARL will be shown to converge to a cooperative strategy faster, with higher overall score on average, and with fewer centralized parameters compared to baselines.

1.1 Related works and their limitations

QMARL is a nascent field, with few works applying the quantum advantage to scenarios with multiple agents (Yun et al., 2022a; 2023b; 2022b; Chen, 2023; Park et al., 2023; Kölle et al., 2024). Further, the application of quantum to split learning (SL) is even newer, with Yun et al. (2023a) being the only prior work. In Yun et al. (2022a) and Yun et al. (2023b), the authors integrate CTDE into actor-critic QMARL to train localized quantum actors with a centralized quantum critic. In Yun et al. (2022b), the authors propose a quantum meta MARL framework which uses a central meta Q-learning agent to train other local agents. The work in Chen (2023) proposes quantum asynchronous advantage actor-critic as a framework for training decentralized QRL agents, which leverages jointly a *global shared memory* and *agent-specific memories* to train parallel agents. The work in Park et al. (2023) proposes a QMARL approach for autonomous mobility cooperation using actor-critic networks with CTDE in noisy intermediate-scale quantum (NISQ) environments with a shared replay buffer. In Kölle et al. (2024), the authors propose a QMARL approach using evolutionary optimization with a VQC design based on quantum classification networks and agent policies implemented as independent VQC models with shared local information. Finally, in Yun et al. (2023a), the authors propose an extension of SL to QML for classification tasks; where local QNN branches send predictions via a classical channel to a central server for cross-channel pooling aggregation.

The resounding theme in Yun et al. (2022a; 2023b; 2022b); Chen (2023); Park et al. (2023); Kölle et al. (2024); Yun et al. (2023a) is the use of independent agents or branches that communicate and learn through centralized classical means. No prior work, however, makes use of the quantum channel as a medium for coupling system elements or for multi-agent collaboration. Indeed, the quantum elements serve as drop-in replacements for classical neural network (NN) counterparts, and, importantly, the quantum channel between agents and the potential for sharing entangled qubit states go largely under-utilized. Simply put, entanglement and the quantum channel are potentially useful untapped cooperative resources intrinsic to QMARL that have largely unknown benefits.

1.2 Contributions

The contributions of this work are summarized as follows:

- We propose a novel eQMARL framework that trains decentralized policies via a split quantum critic over a quantum channel with entangled input qubits and joint measurement.
- We propose a new QMARL algorithm for training distributed agents via optimizing a split critic *without sharing local environment observations amongst agents or a central server*.
- We show that the split nature of eQMARL reduces the computational burden of a central quantum server by distributing and tuning parameterized quantum gates across agents in the system, and requiring a small number of parameters for joint measurement.

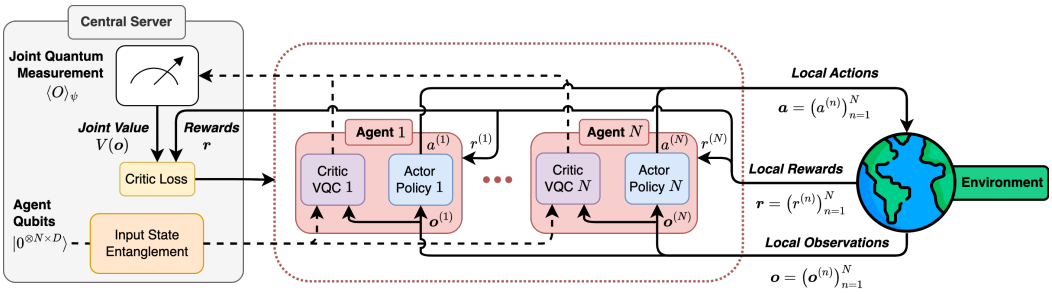

Figure 1: General design of our eQMARL framework. Dashed (solid) arrows represent quantum (classical) communication. A split quantum critic is deployed across the agents via local VQCs (purple) coupled via input entanglement (orange) at a trusted central server (gray). Joint quantum measurements across all qubits (white) estimate the joint value from the locally-encoded observations.

- We empirically demonstrate that eQMARL with Ψ^+ entanglement exhibits a faster convergence time that can reach up to 17.8% faster, and with higher overall score, compared to split classical and fully centralized classical and quantum baselines in environments with full and partial information. Further, the results also show that eQMARL achieves this level of performance and cooperation with a constant factor of 25-times fewer centralized parameters compared to the split classical baseline.

To the best of our knowledge, this is the first application of QMARL that exploits the quantum channel and entanglement between agents to learn without sharing local observations, while also reducing the classical communication overhead and central computation burden of leading approaches.

2 Proposed eQMARL framework

Our proposed eQMARL framework is a new approach for training multi-agent actor-critic architectures which lies at the intersection between CTDE and fully decentralized learning. Inspired from CTDE, we deploy decentralized agent policies which learn using a joint value function at training time. The key to our approach, however, is that we use quantum entanglement to deploy the joint value function estimator as a critic network *which is spread across the agents to operate in mostly decentralized fashion*. An overview of our framework design is shown in Fig. 1, and the design of the system architecture from a purely quantum perspective is shown in Fig. 2. From Fig. 1, the two main elements of eQMARL are a *central quantum server* and a set of N *decentralized quantum agents* $\mathcal{N} = \{n\}_{n=1}^N$. The decentralized agents do not communicate with each other; only communication with the server is necessary during training. During execution, the agents interact with the environment independently and are fully decentralized. During training, our eQMARL framework is divided into core stages: 1) Centralized quantum input state entanglement preparation, 2) Decentralized agent environment observation encoding and variational rotations, and 3) Joint value estimation through joint quantum measurement. Fig. 2 shows how input states are prepared using custom pairwise entanglement operators, followed by agent VQCs, and then joint measurements. Physically, these operations occur at different locations, however, it is equivalent to consider these as a single quantum system, from input state preparation to final measurement. For purposes of quantum state transmission, we assume an ideal quantum channel environment with no losses.

2.1 Joint input entanglement

The first stage of eQMARL creates an entangled input state for the split quantum critic network, which couples the critic VQCs spread across the agents. Each agent $n \in \mathcal{N}$ is assigned a set of D qubits $\mathcal{Q}^{(n)} = \{q_d^{(n)}\}_{d=1}^D$ chosen based upon the environment state dimension and desired quantum state encoding method. The number of qubits is $N \times D$, and is represented by the union of agent qubit sets $\mathcal{Q} = \bigcup_{n=1}^N \mathcal{Q}^{(n)}$. We couple the agents by preparing an input state which pairwise entangles their qubits using a variation of Bell state entanglement (Nielsen & Chuang, 2012) such that

$$\text{ENT}^B_{\delta(1,d),\ldots,\delta(N,d)} = \begin{cases} \left(\bigotimes_{n=2}^N \text{CNOT}_{\delta(1,d),\delta(n,d)}\right) H_{\delta(1,d)}, & \text{if } B = \Phi^+, \\ \left(\bigotimes_{n=2}^N \text{CNOT}_{\delta(1,d),\delta(n,d)}\right) H_{\delta(1,d)} X_{\delta(1,d)}, & \text{if } B = \Phi^-, \\ \left(\bigotimes_{n=2}^N \text{CNOT}_{\delta(1,d),\delta(n,d)}\right) H_{\delta(1,d)} \left(\bigotimes_{k=2}^N X_{\delta(k,d)}\right), & \text{if } B = \Psi^+, \\ \left(\bigotimes_{n=2}^N \text{CNOT}_{\delta(1,d),\delta(n,d)}\right) H_{\delta(1,d)} \left(\bigotimes_{k=1}^N X_{\delta(k,d)}\right), & \text{if } B = \Psi^-, \end{cases} \tag{1}$$

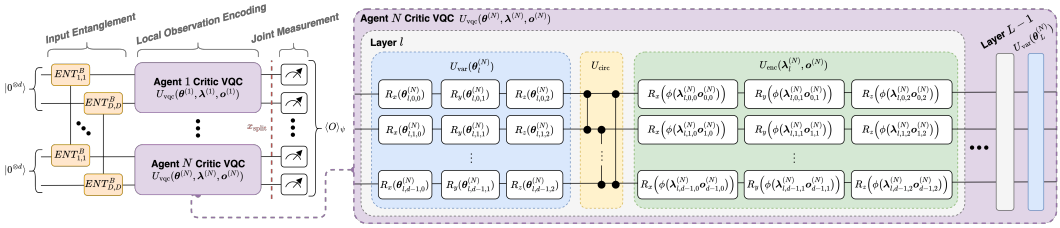

Figure 2: Quantum system design with N agents and D qubits per agent. Input entanglement operators (orange) couple the split critic VQCs (purple, with split point marked in red), which has cascaded layers of variational (blue), circular entanglement (yellow), and encoding (green) operators.

is a coupling operator across qubits $\{q_d^{(n)}\}_{n=1}^{N} \subseteq \mathcal{Q}$, where $\mathcal{B} \in \{\Phi^+, \Phi^-, \Psi^+, \Psi^-\}$ is the set of Bell states, $B \in \mathcal{B}$ is the selected entanglement scheme, $\delta(n,d) = (n-1)D + d$ is an index mapping within $\mathcal{Q}$ for agent $n \in \mathcal{N}$ at qubit index $d \in [1, D]$, i.e., $\delta(n,d) \equiv q_d^{(n)} \in \mathcal{Q}^{(n)}$. Importantly, this operator can be applied to entangle any arbitrary set of qubits within the circuit. Note that in this work we assume the agents receive their entangled qubits in real-time via a trusted central source, i.e., a central server, however, they could be pre-generated and stored in quantum memory at the agent if desired. The quantum circuits that generate each $B \in \mathcal{B}$ are given in Appendix B, Fig. B.1.

2.2 Decentralized split critic VQC design

At its core, our joint quantum critic is a split neural network (SNN) (Vepakomma et al., 2018), with each agent's local VQC serving as a branch. After the input qubits are entangled, they are partitioned back into N sets of D qubits, i.e., $\{\mathcal{Q}^{(n)}\}_{n\in\mathcal{N}}$, and transmitted to each agent respectively. The agents collect and encode local observations from the environment into their assigned qubits using a VQC. We use the VQC architectures of Jerbi et al. (2021); Skolik et al. (2021) for our hybrid quantum network design. Each agent in our QMARL setting uses the same VQC architecture for their branch of the critic, but tunes their own unique set of parameters. The same architecture is a reasonable assumption since all agents are learning in the same environment, and the uniqueness of parameters tailors each branch to local observations. From Fig. 2, the VQC design consists of L cascaded layers of *variational*, *circular entanglement*, and *encoding* operators, with an additional variational layer at the end of the circuit before measurement. The trainable variational layer performs sequential parameterized Pauli X, Y, and Z-axis rotations, and it can be expressed as the unitary operator $U_{\text{var}}(\boldsymbol{\theta}_l^{(n)}) = \bigotimes_{d=0}^{D-1} R_z(\boldsymbol{\theta}_{l,d,2}^{(n)}) R_y(\boldsymbol{\theta}_{l,d,1}^{(n)}) R_x(\boldsymbol{\theta}_{l,d,0}^{(n)})$, where $\boldsymbol{\theta}^{(n)} \in [0, 2\pi]^{(L+1)\times D\times 3}$ is a matrix of rotation angle parameters for agent n. The non-trainable circular entanglement layer binds neighboring qubits within a single agent using the operator $U_{\text{circ}} = CZ_{0,D-1}\big(\prod_{d=0}^{D-2} CZ_{d,d+1}\big)$. The trainable encoding layer maps a matrix of classical features $\boldsymbol{o}^{(n)} \in \mathbb{R}^{D\times 3}$, i.e., an agent's environment observation, into a quantum state via the operator: $U_{\text{enc}}(\boldsymbol{\lambda}_l^{(n)}, \boldsymbol{o}^{(n)}) = \bigotimes_{d=0}^{D-1} R_z\big(\phi(\boldsymbol{\lambda}_{l,d,2}^{(n)} \boldsymbol{o}_{d,2}^{(n)})\big) R_y\big(\phi(\boldsymbol{\lambda}_{l,d,1}^{(n)} \boldsymbol{o}_{d,1}^{(n)})\big) R_x\big(\phi(\boldsymbol{\lambda}_{l,d,0}^{(n)} \boldsymbol{o}_{d,0}^{(n)})\big)$, where $\boldsymbol{\lambda}^{(n)} \in \mathbb{R}^{L\times D\times 3}$ is a matrix of trainable scaling parameters, and $\phi\colon \mathbb{R} \mapsto \mathbb{R}$ is an optional squash activation function. The entire VQC can be expressed as a single operator, as follows:

$$U_{\text{vqc}}(\boldsymbol{\theta}^{(n)}, \boldsymbol{\lambda}^{(n)}, \boldsymbol{o}^{(n)}) = U_{\text{var}}(\boldsymbol{\theta}_L^{(n)}) \prod_{l=0}^{L-1} U_{\text{enc}}(\boldsymbol{\lambda}_{L-l-1}^{(n)}, \boldsymbol{o}^{(n)})\, U_{\text{circ}}\, U_{\text{var}}(\boldsymbol{\theta}_{L-l-1}^{(n)}), \tag{2}$$

which is parameterized by variational angles $\boldsymbol{\theta}^{(n)}$ and encoding weights $\boldsymbol{\lambda}^{(n)}$.

2.3 Centralized joint measurement

The locally encoded qubits for each agent are subsequently forwarded to a central quantum server, which could either be the entanglement source or a different location, for joint measurement. A joint measurement across all qubits in the system is made in the Pauli Z basis using the observable $O = \bigotimes_{d=1}^{N\times D} Z_d$. The joint value for the locally-encoded observations is then estimated as follows:

$$V(\boldsymbol{o}) \simeq w\left(\frac{1 + \langle O\rangle_\psi}{2}\right), \tag{3}$$

where $w \in \mathbb{R}$ is a learned scaling parameter, $\langle O\rangle_\psi$ is the expected value of the joint observable w.r.t. an arbitrary system state $|\psi\rangle$ across all qubits, and $\boldsymbol{o} = (\boldsymbol{o}^{(n)})_{n=1}^{N}$ is a vector of joint observations.

Algorithm 1: Summary of eQMARL training using MAA2C for a quantum entangled split critic. The full algorithm is provided in Appendix C, Algorithm C.1

Require: Set of N agents $\mathcal{N}$, 1 quantum entanglement source, 1 quantum measurement server

Initialize N critic branches U_{vqc} with D qubits and parameters $\boldsymbol{\theta}^{(n)}_{\text{critic}}$, $\boldsymbol{\lambda}^{(n)}$, $\forall n \in \mathcal{N}$;
for *all episodes* **do**
  for *all time steps* τ **do** ▷ `eQMARL training, notation` $\boldsymbol{o}_\tau = \left(\boldsymbol{o}^{(n)}_\tau\right)^N_{n=1}$, $\boldsymbol{o}_{\tau+1} = \left(\boldsymbol{o}^{(n)}_{\tau+1}\right)^N_{n=1}$, $\boldsymbol{a}_\tau = \left(a^{(n)}_\tau\right)^N_{n=1}$.
    Central quantum server generates $2N$ sets of D entangled qubits and sends to agents via **quantum channel**;
    for *each agent* $n \in \mathcal{N}$ **do**
      Apply $U_{\text{vqc}}(\boldsymbol{\theta}^{(n)}_{\text{critic}}, \boldsymbol{\lambda}^{(n)}, \boldsymbol{o}^{(n)}_\tau)$ and $U_{\text{vqc}}(\boldsymbol{\theta}^{(n)}_{\text{critic}}, \boldsymbol{\lambda}^{(n)}, \boldsymbol{o}^{(n)}_{\tau+1})$ from (2) locally using assigned entangled input qubits;
      Transmit resulting qubits via **quantum channel**, and reward $r^{(n)}_\tau$ via **classical channel** to central quantum server;
    end
    Perform joint measurements on qubits across all agents to estimate $V(\boldsymbol{o}_\tau)$ and $V(\boldsymbol{o}_{\tau+1})$ using (3);
    Estimate $Q(\boldsymbol{o}_\tau, \boldsymbol{a}_\tau) = \sum_{n=1}^N r^{(n)}_\tau + \gamma V(\boldsymbol{o}_{\tau+1})$ using discount factor γ;
    Compute $\nabla_{x_{\text{split}}} \mathcal{L}_{\text{critic}}$ and transmit via **classical channel** to each agent to update $\boldsymbol{\theta}^{(n)}_{\text{critic}}$ locally using partial gradient from (4);
  end
end

This rescaling is necessary because the range of the measured observable is $\langle O \rangle_\psi \in [-1, 1]$ (i.e., proportional to the eigenvalues of the operator O), whereas $V(\boldsymbol{o}) \in \mathbb{R}$. The critic loss with respect to the joint value and local agent rewards is then disseminated amongst the agents for tuning of their localized portion of the split critic network and local policy networks.

2.4 Split critic loss

The loss of the split critic is derived in a way similar to Vepakomma et al. (2018). Since the input entanglement stage of eQMARL has no trainable parameters, it does not exist for the purposes of SL backpropagation. We denote the point of joint quantum measurement as the *split point*, which is preceded by local agent VQC *branches*. Each branch can be individually tuned using the partial gradient of the loss at the split point via partial gradient w.r.t. its own local parameters. If we define x_{split} as the split point, then the partial gradient of each branch's parameters can be estimated using the central loss, as follows:

$$\nabla_{\boldsymbol{\theta}^{(n)}_{\text{critic}}} \mathcal{L}_{\text{critic}} = \frac{\partial \mathcal{L}_{\text{critic}}}{\partial \boldsymbol{\theta}^{(n)}_{\text{critic}}} = \frac{\partial \mathcal{L}_{\text{critic}}}{\partial x_{\text{split}}} \frac{\partial x_{\text{split}}}{\partial \boldsymbol{\theta}^{(n)}_{\text{critic}}} = \underbrace{\left(\nabla_{x_{\text{split}}} \mathcal{L}_{\text{critic}}\right)}_{\text{Central server}} \underbrace{\left(\nabla_{\boldsymbol{\theta}^{(n)}_{\text{critic}}} x_{\text{split}}\right)}_{\text{Local agent}}, \tag{4}$$

where $\nabla_{x_{\text{split}}} \mathcal{L}_{\text{critic}}$ is the gradient of the loss at the split point, and $\nabla_{\boldsymbol{\theta}^{(n)}_{\text{critic}}} x_{\text{split}}$ is the gradient from the split point back to the start of branch $n \in \mathcal{N}$. The value of $\nabla_{x_{\text{split}}} \mathcal{L}_{\text{critic}}$ is sent classically to the agents, and since (3) only uses a single trainable parameter, w, the classical communication overhead needed for split backpropagation is minimal. Here, we use the `Huber` loss for the critic (see Appendix D).

2.5 Coupled agent learning algorithm

Our eQMARL uses a variation of the multi-agent advantage actor-critic (MAA2C) algorithm (Papoudakis et al., 2021) to train local agent policies with a split quantum joint critic. Here, we summarize the algorithm in Algorithm 1, which focuses on the elements for necessary for tuning the critic. In eQMARL, there are N quantum agents that are physically separated from each other (no cross-agent communication is assumed) and one central quantum server. Each agent $n \in \mathcal{N}$ employs a VQC, given by (2), with unique parameters $\boldsymbol{\theta}^{(n)}_{\text{critic}}$ and $\boldsymbol{\lambda}^{(n)}$, that serves as one branch in the split critic network. All agents interact with the environment independently and each has its own local data buffer – local observations are neither shared amongst agents nor with the server. The first stage of eQMARL is fundamentally similar to traditional MAA2C. The second stage is where the uniqueness of eQMARL comes into play. The central quantum server prepares $2N$ sets of D entangled qubits using (1) for each time step τ, which are then transmitted to the agents via a quantum channel. Each agent then encodes their local observations $\boldsymbol{o}^{(n)}_\tau$ and $\boldsymbol{o}^{(n)}_{\tau+1}$ using (2) and their assigned entangled input qubits, and transmits the resulting qubits via quantum channel back to the server. The agents also share their corresponding reward $r^{(n)}_\tau$ via a classical channel with the server, which will be used for downstream loss calculations. Access to the reward is necessary for the critic to evaluate agent policy performance. This is a reasonable assumption in eQMARL as the reward value contains no localized environment information, and is also used in Yun et al. (2022a; 2023b); Park et al. (2023); regardless, the classical channel will also be used to transmit partial gradients of

the critic loss. The server then performs a joint measurement on all the qubits associated with $\boldsymbol{o}_\tau^{(n)}$ and $\boldsymbol{o}_{\tau+t}^{(n)}$ to obtain estimates for $V(\boldsymbol{o}_\tau)$ and $V(\boldsymbol{o}_{\tau+1})$ using (3). Subsequently, the server computes the expected cumulative reward $Q(\boldsymbol{o}_\tau, \boldsymbol{a}_\tau)$ for the joint observations and actions at τ using $V(\boldsymbol{o}_{\tau+1})$, discount factor γ, and the respective rewards. The joint critic loss $\mathcal{L}_{\text{critic}}$ is then computed, its partial gradient w.r.t. the split point $\nabla_{x_{\text{split}}}\mathcal{L}_{\text{critic}}$ is estimated, and then sent via a classical channel to each agent to update their local weights $\boldsymbol{\theta}_{\text{critic}}^{(n)}$ using (4).

3 Experiments and demonstrations

3.1 Environments

We use the `CoinGame` environment first proposed in Lerer & Peysakhovich (2018), and as implemented in Phan et al. (2022), which has been widely used (Foerster et al., 2018; Phan et al., 2022; Kölle et al., 2024), and a multi-agent variant of the canonical `CartPole` environment (Barto et al., 1983) as benchmarks for MARL scenarios. In particular, `CoinGame`'s nature as a zero-sum game and the independent nature of multi-agent `CartPole` serve as intriguing case studies for learning cooperative strategies using full, i.e., described by a Markov decision process (MDP), and partial, i.e., described by a partially observable MDP (POMDP), information. In `CoinGame`, we evaluate agents using three metrics: 1) *Score*, which aggregates all agent undiscounted rewards over a single episode, 2) *Total coins collected*, which provides insight into how active the agents were during the game, and 3) *Own coin rate*, which sheds light on how the agents achieve cooperation, specifically by being selective on which coins they procure. In multi-agent `CartPole`, we evaluate agents using the *total reward* metric, which aggregates the number of time steps an agent is able to maintain pole balance over a single episode. See Appendix E for environment details.

3.2 Experiment setup

We compare eQMARL against three baselines that considered the current state-of-the-art configurations in actor-critic CTDE: 1) **Fully centralized CTDE (fCTDE)**, a purely classical configuration where the critic is a simple fully-connected NN located at a central server, like in Gupta et al.; Foerster et al., and requires agents to transmit their local observations to the central server via a classical channel; 2) **Split CTDE (sCTDE)**, is another purely classical configuration where the critic is a branching classical NN encoder spread across the agents, and the central server contains a classical NN based on Rashid et al. (2018); and 3) **Quantum fully centralized CTDE (qfCTDE)**, a quantum variant of fCTDE where the critic is located at a central server, as in Yun et al. (2022a; 2023b); Park et al. (2023), and requires agents to transmit their local observations via a classical channel. These baselines were specifically chosen to convey how a quantum entangled split critic eliminates the transfer of local environment observations, while reducing classical communication overhead by leveraging the quantum channel, and minimizing centralized computational complexity. In our experiments we simplify the setup by using policy sharing across the agents, as done in Yun et al. (2023b) and Chen (2023). All classical models were built using `tensorflow`, the quantum models using `tensorflow-quantum`, and `cirq` for quantum simulations. For `CoinGame`, all models were trained for 3000 epochs, with $T = 50$ steps, $\gamma = 0.99$. For `CartPole`, all models were trained for 1000 epochs, with a maximum of 500 steps per episode. All models use the `Adam` optimizer with varying learning rates. The quantum models use $D = 4$ qubits, $L = 5$ layers, and $\phi = \texttt{arctan}$ activation. The classical models use $h = 12$ hidden units. See Appendices F to H for further details.

3.3 Comparing quantum input entanglement styles

The first set of experiments demonstrate the effectiveness of various input entanglement styles used for our eQMARL approach. We run two separate experiments using the `CoinGame-2` environment with both full and partial information. The score metric results for both dynamics are shown in Fig. 3. We specifically consider score thresholds of 20 and 25 which serve as markers to aid our discussion. In the MDP setting of Fig. 3a, we can see see that Ψ^+ entanglement achieves a score value of 20 at epoch 568, which is 4.5% faster than Ψ^-. Similarly, a score of 25 is achieved by Φ^+ at epoch 1883, which is 5.2% faster than Ψ^-. At the end of training, all peak scores hover slightly above 25. Looking at the shaded standard deviation regions, we get a sense for the stability of each entanglement style. Specifically, we see that Ψ^+, Ψ^-, and Φ^+ have similar tight ranges until epoch 1500, whereas both Φ^- and `None` have far lower minimum values until around epoch 1300.

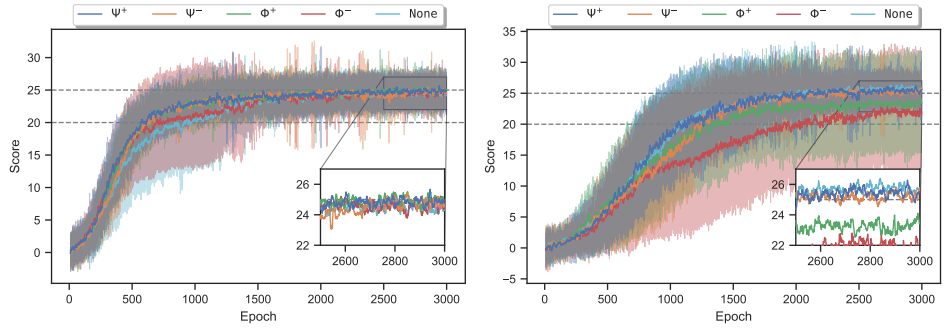

(a) Score - MDP (b) Score - POMDP

Figure 3: Comparison of `CoinGame-2` score performance with (a) MDP, and (b) POMDP dynamics for `eQMARL` using Ψ^+ (blue), Ψ^- (orange), Φ^+ (green), Φ^- (red), and `None` (cyan) entanglement averaged over 10 runs, with ± 1 std. dev. shown as shaded regions. These figures generally show that Ψ^+ outperforms other entanglement styles across both environment dynamics.

Moreover, Ψ^- appears to have large downward spikes toward the end of training. Fig. 3a shows that there is a gap in convergence between Φ^- and `None`, and the other styles. Looking closer, we observe that Φ^+ plateaus at earlier epochs, and Ψ^- is more unstable (dropping in score) at later epochs. Hence, *we see a clear advantage for applying* Ψ^+. In the POMDP setting of Fig. 3b, we see that Ψ^+ achieves a score of 20 at epoch 1049, which is about 2% faster than `None`. Interestingly, there is a much larger gap in convergence between Φ^- and the others. A score of 25 is achieved by Ψ^+ at epoch 1745, a 10.7% increase over `None`, whereas both Φ^+ and Φ^- never reach this threshold. The final peak scores for Ψ^+ and `None` hover slightly above 26. The shaded standard deviation regions exhibit a cascade effect between the styles, and, in particular, we observe that Φ^- has the lowest min, followed by Φ^+ which has a slightly higher floor. These groupings are interesting as both Φ^+ and Φ^- are similar in composition, only differing by a phase. Hence, *we again see a clear convergence and score advantage for using* Ψ^+.

Comparing the performance of the entanglement styles with both dynamics paints a picture of the generalizability of the system as a whole. Interestingly, the worse performance of Φ^+ and Φ^- suggests that same-state entanglement, $|00\rangle$ and $|11\rangle$, regardless of phase, results in less coupling of agents compared to opposite-state entanglement, $|01\rangle$ and $|10\rangle$. The consistently high performance of Ψ^+ in both dynamics suggests that it enhances the generalizability of the system, and, since input entanglement does not increase classical computational overhead, we see that Ψ^+ entanglement can be used to couple the agents in both dynamics while achieving comparable or higher performance. Thus, *we select* Ψ^+ *as the entanglement scheme to be used in all subsequent experiments*.

3.4 CoinGame EXPERIMENTS

We next compare the performance of `eQMARL-`Ψ^+ with baselines `fCTDE`, `sCTDE`, and `qfCTDE` using the `CoinGame-2` environment with MDP state dynamics, as shown in Figs. 4a and 4c. Initially inspecting both score (Fig. 4a) and own coin rate (Fig. 4c) metrics, we can readily see that `eQMARL-`Ψ^+ achieves higher performance with short convergence time. Looking at the score metric in Fig. 4a, we see that `eQMARL-`Ψ^+ achieves a score of 20 at epoch 568, and *it converges* 16.2% *faster than the next closest* `qfCTDE`. A score threshold of 25 is reached by `eQMARL-`Ψ^+ at epoch 2332, and *it clearly converges* 10.8% *faster than* `sCTDE`. Overall, we observe a 1.4% increase in max score for `eQMARL-`Ψ^+ compared to the next highest `sCTDE`. Additionally, `eQMARL-`Ψ^+ is smoother than `qfCTDE` at later epochs; suggesting that input entanglement stabilizes convergence. Fig. 4c shows the score in terms of own coin rate, which demonstrates how a cooperative strategy is achieved. We use thresholds of 0.95 and 1.0 as markers to gauge performance. From Fig. 4c, we observe that `eQMARL-`Ψ^+ rapidly achieves a 0.95 rate at epoch 376, and converges to a rate of 1.0 at epoch 2136. In other words, nearly all the coins each agent collected in the games were of their corresponding color. In contrast, `sCTDE`, `fCTDE`, and `qfCTDE` converge at a much slower pace, never achieve a rate of 1.0, and exhibit greater fluctuation at the end of the training. From this, we observe that `eQMARL-`Ψ^+ *converges to a* 0.95 *rate* 5.3% *faster than* `qfCTDE`*, and is the only one to achieve a* 1.0 *rate*. Additionally, we also see that the `eQMARL-`Ψ^+ rate curve is smoother than all of the other approaches at later epochs, similar to the score metric.

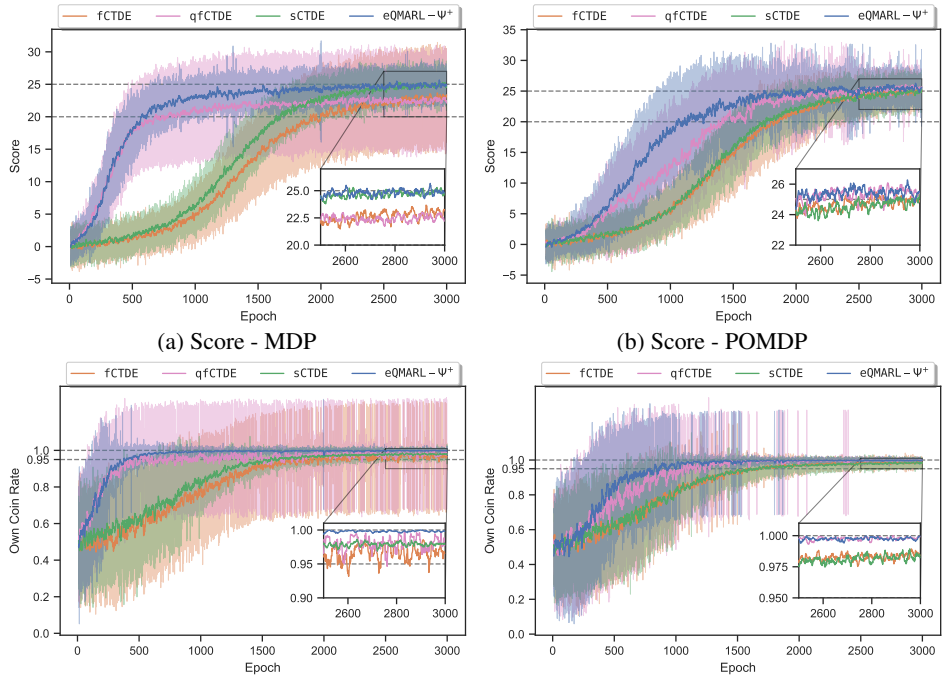

(a) Score - MDP (b) Score - POMDP

(c) Own coin rate - MDP (d) Own coin rate - POMDP

Figure 4: Comparison of `CoinGame-2` MDP and POMDP environment (a,b) score, and (c,d) own coin rate performance for `fCTDE` (orange), `qfCTDE` (magenta), `sCTDE` (green), and `eQMARL-`Ψ^+ (blue) averaged over 10 runs, with ± 1 std. dev. shown as shaded regions. These figures generally show that eQMARL outperforms baselines across both environment dynamics.

From Figs. 4a and 4c, we conclude that *our proposed `eQMARL-`Ψ^+ configuration learns to play the game significantly faster than the classical variants* without sharing local observations, transmitting intermediate activations, nor tuning large NNs at the central server. The higher performance and shorter convergence time compared to `qfCTDE` and both classical `fCTDE` and `sCTDE` approaches shows that splitting the critic amongst the agents results in no apparent loss in capability. In fact, the smoothness of the curves suggests that the input entanglement stabilizes the network over time. Further, the own coin rate performance shows that `eQMARL-`Ψ^+ learns a cooperative strategy significantly faster than the classical approaches, and with less fluctuation than `qfCTDE`.

Figs. 4b and 4d show the results of the `CoinGame-2` environment with POMDP state dynamics. Fig. 4b shows that `eQMARL-`Ψ^+ achieves a score value of 20 at epoch 1049, which clearly converges 24% faster considering the noticeable gap between it and `qfCTDE`. This demonstrates that the branching quantum network with input entanglement shortens convergence time compared to the fully centralized variant Fig. 4b also shows that all models achieve a score of 25, however, in this case, `eQMARL-`Ψ^+ converges 17.8% faster and with slightly higher score than `qfCTDE`. Examining smoothness, we see much greater fluctuation between all curves compared to the MDP case. Fig. 4d shows that `eQMARL-`Ψ^+ achieves a 0.95 rate rapidly at epoch 773, *converging* 25.5% *faster than `qfCTDE` as the next closest*. Notice how `qfCTDE` specifically exhibits greater fluctuation until the 0.95 rate is achieved. This again suggests that the addition of input entanglement and splitting the quantum critic contribute to smoother convergence. The convergence near threshold 1.0 paints an interesting picture. We see that `qfCTDE` actually achieves a perfect 1.0 rate at epoch 2887, whereas `eQMARL-`Ψ^+, `sCTDE`, and `fCTDE` never reach this rate; with the highest max value being 0.9996 for `eQMARL-`Ψ^+ at epoch 2533. This is interesting because, despite `qfCTDE` achieving a higher rate, *`eQMARL-`Ψ^+ converges to nearly the same rate* 12.3% *faster*. This demonstrates the convergence advantages of incorporating input entanglement into the quantum models while simultaneously splitting the critic amongst the agents over a quantum channel.

The difference in performance between the baselines in Figs. 4b and 4d demonstrates a clear quantum advantage for learning in the presence of partial information. Specifically, the faster convergence to peak score and own coin rate thresholds in `eQMARL-`Ψ^+ demonstrates that splitting the quantum critic across the quantum channel with entangled input qubits allows the agents to learn a more cooperative strategy without direct access to local observations. This is interesting because `qfCTDE`

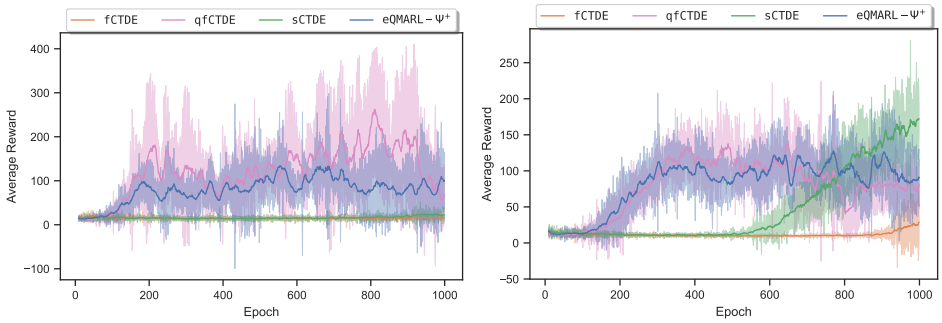

(a) Average Reward - MDP (b) Average Reward - POMDP

Figure 5: Comparison of `CartPole` MDP and POMDP environment average reward performance for `fCTDE` (orange), `qfCTDE` (magenta), `sCTDE` (green), and `eQMARL-`Ψ^+ (blue) averaged over 5 runs of 1000 epochs, with ± 1 std. dev. shown as shaded regions. These figures generally show that eQMARL outperforms classical baselines and is more stable than `qfCTDE` across both dynamics.

is centralized and has all local observations at its disposal. This additional information would initially suggest better performance compared to approaches with only local information. However, from Figs. 4b and 4d, we observe a clear benefit for not only splitting the quantum critic as branches across the agents, but also introducing an entangled input state that couples their encoding behavior.

3.5 CartPole Experiments

The next set of experiments compare the performance of eQMARL with baselines using a multi-agent variant of the `CartPole` environment with both MDP and POMDP state dynamics. The average reward metric across all agents in the environment for both dynamics is shown in Fig. 5. We use reward thresholds of the *mean* and *max* values to draw comparisons. From Fig. 5 we see that the classical models do not perform well overall in either setting, and `qfCTDE` experiences high variance in the MDP case. For MDP, `qfCTDE` achieves the highest mean (121.35 at epoch 189) and max (262.43 at epoch 810) rewards overall, but does so with an extremely high standard deviation of 110.13. In contrast, `eQMARL-`Ψ^+ achieves its mean reward of 79.11 at epoch 166, and max reward of 134.16 at epoch 555, which are 12.2% and 31.5% faster than `qfCTDE` respectively. For POMDP, we see that `sCTDE` achieves the highest overall max reward of 172.16 at epoch 998, but with a very low mean of 47.59 at epoch 669. In contrast, `qfCTDE` achieves a max value 137.66 at epoch 648, compared to `eQMARL-`Ψ^+ with max 127.60 at epoch 770. `eQMARL-`Ψ^+ achieves the highest mean reward 82.28 at epoch 251, which is 9.1% faster than `qfCTDE` (mean 79.03 at epoch 276) with a similarly low standard deviation to the MDP setting.

The key observation from the `CartPole` experiments is that `eQMARL-`Ψ^+ more rapidly learns a strategy with higher average reward than the classical variants in both MDP and POMDP settings. Further, `eQMARL-`Ψ^+ slightly outperforms `qfCTDE` in the POMDP setting with a higher average reward, and is much more stable with a significantly lower variance in the MDP setting – all achieved via implicit collaboration though entanglement. These results show that, without observation sharing, `eQMARL-`Ψ^+ can learn a similarly performant, and dramatically more stable, strategy compared to a fully centralized quantum approach that has access to all agent observations.

3.6 Ablation Study

The last set of experiments we consider is an ablation study to examine the relationship between NN layer depth and performance, and to facilitate fair model size comparisons. In particular, we trained `fCTDE` and `sCTDE` with hidden layer units $h \in \{3, 6, 12, 24\}$, and `qfCTDE` and `eQMARL` with VQC layers $L \in \{2, 5, 10\}$ on the `CoinGame-2` environment with MDP and POMDP state dynamics for 10 experiments of 3000 epochs each. An excerpt of the score metrics results for `eQMARL` and `sCTDE` in the MDP setting are shown in Fig. 6, and a comparison of the critic model sizes used in each framework is shown in Table 1. The full results are provided in Appendix H.4.

In Fig. 6 we see that `eQMARL-`Ψ^+ with $L = 5$ achieves a mean score 3-times higher than $L = 2$, and nearly identical to $L = 10$. This trend is similar for `qfCTDE`. Both `sCTDE` and `fCTDE` also exhibit similar behavior for hidden units; that is the performance of $h = 12$ is nearly 2-times that of $h = 6$, and only marginally less than $h = 24$. Considering the significant performance drops and increased variation incurred by reducing, and the limited gains by increasing, both h and L, the selection of

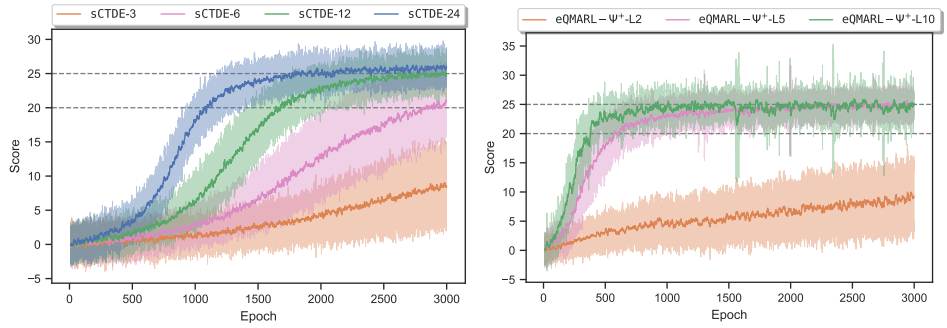

(a) sCTDE (b) eQMARL-Ψ^+

Figure 6: Ablation study score performance on MDP CoinGame-2 for (a) sCTDE, and (b) eQMARL-Ψ^+ with hidden layer units $h \in \{3, 6, 12, 24\}$ and VQC layers $L \in \{2, 5, 10\}$, averaged over 10 runs of 3000 epochs, with ± 1 std. dev. shown as shaded regions. These figures generally show that selecting parameters $h = 12$ and $L = 5$ results in optimal performance.

Table 1: Comparison of the best critic model size in number of trainable parameters for each framework used on the CoinGame-2 environment with MDP and POMDP dynamics.

Framework	Ablation Selection	Number of critic parameters: MDP	Number of critic parameters: POMDP
eQMARL	$L = 5$	265 (132 per agent, 1 central)	817 (408 per agent, 1 central)
qfCTDE	$L = 5$	265	817
fCTDE	$h = 12$	889	673
sCTDE	$h = 12$	913 (444 per agent, 25 central)	697 (336 per agent, 25 central)

$h = 12$ and $L = 5$ results in the most comparable performance across all baselines. Looking at Table 1, the critic sizes reported are for the entire system. This distinction is important since both eQMARL and sCTDE split the critic network across the agents the total size of the agent-specific network is a fraction of the total size. For MDP dynamics, we observe that the quantum models are smaller than the classical variants by about a factor of 4. For POMDP, we observe that the quantum models are slightly larger overall than their classical counterparts. This is because, in POMDP, the quantum models require a classical NN for dimensionality reduction at the input of each encoder. While the overall system size is larger, however, the number of central parameters is significantly reduced in the quantum cases – requiring only 1 parameter instead of 25. This is important for scaleability because the classical cases implement a full NN at the central server and its size scales with N. In contrast, the quantum network only has a single trainable parameter tied to the measurement observable, which will remain fixed regardless of N.

4 Conclusion

In this paper we have proposed eQMARL, a novel quantum actor-critic framework for training decentralized policies using a split quantum critic with entangled input qubits and joint measurement. Spreading the critic across the agents via a quantum channel eliminates sharing local observations, minimizes the classical communication overhead from sending model parameters or intermediate NN activations, and reduces the centralized classical computational burden through optimization of a single quantum measurement observable parameter. We have shown that Ψ^+ input entanglement improves agent cooperation and system generalizability across both MDP and POMDP environments. For MDP, we have shown that eQMARL converges to a cooperative strategy 10.8% faster and with a higher score compared to sCTDE. Likewise, for POMDP, we have shown that eQMARL converges to a cooperative strategy 17.8% faster and with slightly higher score compared to qfCTDE. Further, we have also shown that eQMARL outperforms classical baselines and exhibits more stable performance than qfCTDE in completely independent environments. Lastly, we have shown that eQMARL requires 25-times fewer centralized parameters compared to sCTDE. One limitation of this work is the computational complexity of quantum simulations on classical hardware, which is an ongoing topic of research for NISQ systems of many qubits. Indeed, many recent works on QMARL (Yun et al., 2022a; 2023b; 2022b; Chen, 2023; Park et al., 2023; Kölle et al., 2024) have similar hardware requirements to ours. Further, many recent works on quantum networks (Van Meter et al., 2022; Pettit et al., 2023; Lei et al., 2023; Azuma et al., 2023) propose methods for generating and storing entangled qubits, which can be used to support the type of entanglement required in our system.

REFERENCES

Koji Azuma, Sophia E. Economou, David Elkouss, Paul Hilaire, Liang Jiang, Hoi-Kwong Lo, and Ilan Tzitrin. Quantum repeaters: From quantum networks to the quantum internet. *Reviews of Modern Physics*, 95(4):045006, December 2023. ISSN 0034-6861, 1539-0756. doi: 10.1103/RevModPhys.95.045006. URL https://link.aps.org/doi/10.1103/RevModPhys.95.045006.

Andrew G. Barto, Richard S. Sutton, and Charles W. Anderson. Neuronlike adaptive elements that can solve difficult learning control problems. *IEEE Transactions on Systems, Man, and Cybernetics*, SMC-13(5):834–846, September 1983. ISSN 2168-2909. doi: 10.1109/TSMC.1983.6313077. URL https://ieeexplore.ieee.org/document/6313077.

Max Born. Quantenmechanik der stoßvorgänge. *Zeitschrift für Physik*, 38(11):803–827, November 1926.

Samuel Yen-Chi Chen. Asynchronous training of quantum reinforcement learning, January 2023. URL http://arxiv.org/abs/2301.05096.

Yuxuan Du, Min-Hsiu Hsieh, Tongliang Liu, and Dacheng Tao. The Expressive Power of Parameterized Quantum Circuits. *Physical Review Research*, 2(3):033125, July 2020. ISSN 2643-1564. doi: 10.1103/PhysRevResearch.2.033125. URL http://arxiv.org/abs/1810.11922.

A. Einstein, M. Born, and H. Born. *The Born-Einstein Letters: Correspondence between Albert Einstein and Max and Hedwig Born from 1916-1955, with Commentaries by Max Born*. Macmillan, 1971. ISBN 978-0-333-11267-0. URL https://books.google.com/books?id=HvZAAQAAIAAJ.

Frederik F. Flöther. The state of quantum computing applications in health and medicine. *Research Directions: Quantum Technologies*, pp. 1–21, July 2023. ISSN 2752-9444. doi: 10.1017/qut.2023.4. URL http://arxiv.org/abs/2301.09106.

Jakob Foerster, Gregory Farquhar, Triantafyllos Afouras, Nantas Nardelli, and Shimon Whiteson. Counterfactual multi-agent policy gradients. 32(1). ISSN 2374-3468, 2159-5399. doi: 10.1609/aaai.v32i1.11794. URL https://ojs.aaai.org/index.php/AAAI/article/view/11794.

Jakob N. Foerster, Richard Y. Chen, Maruan Al-Shedivat, Shimon Whiteson, Pieter Abbeel, and Igor Mordatch. Learning with Opponent-Learning Awareness, September 2018. URL http://arxiv.org/abs/1709.04326.

Jayesh K. Gupta, Maxim Egorov, and Mykel Kochenderfer. Cooperative multi-agent control using deep reinforcement learning. In Gita Sukthankar and Juan A. Rodriguez-Aguilar (eds.), *Autonomous Agents and Multiagent Systems*, volume 10642, pp. 66–83. Springer International Publishing. ISBN 9783319716817 9783319716824. doi: 10.1007/978-3-319-71682-4_5. URL http://link.springer.com/10.1007/978-3-319-71682-4_5.

Dylan Herman, Cody Googin, Xiaoyuan Liu, Alexey Galda, Ilya Safro, Yue Sun, Marco Pistoia, and Yuri Alexeev. A Survey of Quantum Computing for Finance, June 2022. URL http://arxiv.org/abs/2201.02773.

Sofiene Jerbi, Casper Gyurik, Simon C. Marshall, Hans J. Briegel, and Vedran Dunjko. Parametrized quantum policies for reinforcement learning. March 2021. doi: 10.48550/arXiv.2103.05577. URL http://arxiv.org/abs/2103.05577.

Michael Kölle, Felix Topp, Thomy Phan, Philipp Altmann, Jonas Nüßlein, and Claudia Linnhoff-Popien. Multi-Agent Quantum Reinforcement Learning using Evolutionary Optimization, January 2024. URL http://arxiv.org/abs/2311.05546.

Yisheng Lei, Faezeh Kimiaee Asadi, Tian Zhong, Alexander Kuzmich, Christoph Simon, and Mahdi Hosseini. Quantum Optical Memory for Entanglement Distribution, 2023. URL https://arxiv.org/abs/2304.09397.

Adam Lerer and Alexander Peysakhovich. Maintaining cooperation in complex social dilemmas using deep reinforcement learning, March 2018. URL http://arxiv.org/abs/1707.01068.

Fabrizio Logiurato and Augusto Smerzi. Born Rule and Noncontextual Probability. *Journal of Modern Physics*, 03(11):1802–1812, 2012. ISSN 2153-1196. doi: 10.4236/jmp.2012.311225.

Lluís Masanes, Thomas D. Galley, and Markus P. Müller. The measurement postulates of quantum mechanics are operationally redundant. *Nature Communications*, 10(1), March 2019. doi: 10.1038/s41467-019-09348-x. URL https://doi.org/10.1038%2Fs41467-019-09348-x.

Kosuke Mitarai, Makoto Negoro, Masahiro Kitagawa, and Keisuke Fujii. Quantum Circuit Learning. *Physical Review A*, 98(3):032309, September 2018. ISSN 2469-9926, 2469-9934. doi: 10.1103/PhysRevA.98.032309. URL http://arxiv.org/abs/1803.00745.

Bhaskara Narottama, Zina Mohamed, and Sonia Aïssa. Quantum machine learning for next-G wireless communications: Fundamentals and the path ahead. *IEEE Open Journal of the Communications Society*, 4:2204–2224, 2023. doi: 10.1109/OJCOMS.2023.3309268.

Michael A. Nielsen and Isaac L. Chuang. *Quantum Computation and Quantum Information: 10th Anniversary Edition*. Cambridge University Press, 1 edition, June 2012. ISBN 978-1-107-00217-3 978-0-511-97666-7. doi: 10.1017/CBO9780511976667. URL https://www.cambridge.org/core/product/identifier/9780511976667/type/book.

Georgios Papoudakis, Filippos Christianos, Lukas Schäfer, and Stefano V. Albrecht. Benchmarking Multi-Agent Deep Reinforcement Learning Algorithms in Cooperative Tasks, November 2021. URL http://arxiv.org/abs/2006.07869.

Soohyun Park, Jae Pyoung Kim, Chanyoung Park, Soyi Jung, and Joongheon Kim. Quantum Multi-Agent Reinforcement Learning for Autonomous Mobility Cooperation, August 2023. URL http://arxiv.org/abs/2308.01519.

Robert M. Pettit, Farhang Hadad Farshi, Sean E. Sullivan, Álvaro Véliz-Osorio, and Manish Kumar Singh. A perspective on the pathway to a scalable quantum internet using rare-earth ions. *Applied Physics Reviews*, 10(3):031307, September 2023. ISSN 1931-9401. doi: 10.1063/5.0156874. URL https://pubs.aip.org/apr/article/10/3/031307/2906226/A-perspective-on-the-pathway-to-a-scalable-quantum.

Thomy Phan, Felix Sommer, Philipp Altmann, Fabian Ritz, Lenz Belzner, and Claudia Linnhoff-Popien. Emergent cooperation from mutual acknowledgment exchange. In *Proceedings of the 21st International Conference on Autonomous Agents and Multiagent Systems*, AAMAS '22, pp. 1047–1055, Richland, SC, 2022. International Foundation for Autonomous Agents and Multiagent Systems. ISBN 978-1-4503-9213-6.

Tabish Rashid, Mikayel Samvelyan, Christian Schroeder de Witt, Gregory Farquhar, Jakob Foerster, and Shimon Whiteson. QMIX: Monotonic Value Function Factorisation for Deep Multi-Agent Reinforcement Learning, June 2018. URL http://arxiv.org/abs/1803.11485.

Andrea Skolik, Sofiene Jerbi, and Vedran Dunjko. Quantum agents in the Gym: A variational quantum algorithm for deep Q-learning. March 2021. doi: 10.22331/q-2022-05-24-720. URL http://arxiv.org/abs/2103.15084.

Rodney Van Meter, Ryosuke Satoh, Naphan Benchasattabuse, Kentaro Teramoto, Takaaki Matsuo, Michal Hajdusek, Takahiko Satoh, Shota Nagayama, and Shigeya Suzuki. A Quantum Internet Architecture. In *2022 IEEE International Conference on Quantum Computing and Engineering (QCE)*, pp. 341–352, Broomfield, CO, USA, September 2022. IEEE. ISBN 978-1-66549-113-6. doi: 10.1109/QCE53715.2022.00055. URL https://ieeexplore.ieee.org/document/9951258/.

Praneeth Vepakomma, Otkrist Gupta, Tristan Swedish, and Ramesh Raskar. Split learning for health: Distributed deep learning without sharing raw patient data. December 2018. URL http://arxiv.org/abs/1812.00564.

Won Joon Yun, Yunseok Kwak, Jae Pyoung Kim, Hyunhee Cho, Soyi Jung, Jihong Park, and Joongheon Kim. Quantum Multi-Agent Reinforcement Learning via Variational Quantum Circuit Design, March 2022a. URL http://arxiv.org/abs/2203.10443.

Won Joon Yun, Jihong Park, and Joongheon Kim. Quantum Multi-Agent Meta Reinforcement Learning. August 2022b. URL http://arxiv.org/abs/2208.11510.

Won Joon Yun, Hankyul Baek, and Joongheon Kim. Quantum Split Neural Network Learning using Cross-Channel Pooling, April 2023a. URL http://arxiv.org/abs/2211.06524.

Won Joon Yun, Jae Pyoung Kim, Soyi Jung, Jae-Hyun Kim, and Joongheon Kim. Quantum Multi-Agent Actor-Critic Neural Networks for Internet-Connected Multi-Robot Coordination in Smart Factory Management. January 2023b. doi: 10.48550/arXiv.2301.04012. URL https://arxiv.org/abs/2301.04012.

A More comprehensive preliminaries

A.1 Quantum mutli-agent reinforcement learning

We consider a reinforcement learning (RL) setting with multiple agents in environments with both full and partial information. The dynamics of a system with full information is described by a Markov game with an underlying MDP with tuple $M_{\text{MDP}} = \langle \mathcal{N}, \mathcal{S}, \mathcal{A}, \mathcal{P}, \mathcal{R} \rangle$ where $\mathcal{N}$ is a set of N agents, $\mathcal{S} = \{\mathcal{S}^n\}_{n \in \mathcal{N}}$ is the set of joint states across all agents, $\mathcal{A} = \{\mathcal{A}^{(n)}\}_{n \in \mathcal{N}}$ is the set of joint actions, $\mathcal{S}^{(n)}$ and $\mathcal{A}^{(n)}$ are the set of states and actions for agent n, $\mathcal{P}(s_{t+1}|s_t, a_t)$ is the state transition probability, and $\mathcal{R}(s_t, a_t) = \{r_t^{(n)}\}_{n \in \mathcal{N}} \in \mathbb{R}^N$ is the joint reward $\forall s_t \in \mathcal{S}, a_t \in \mathcal{A}$. The dynamics of a system with partial information is described by a Markov game with an underlying POMDP with tuple $M_{\text{POMDP}} = \langle \mathcal{N}, \mathcal{S}, \mathcal{A}, \mathcal{P}, \mathcal{R}, \Omega, \mathcal{O} \rangle$ where $\mathcal{N}, \mathcal{S}, \mathcal{A}, \mathcal{P}$ are the same as in M_{MDP}, however the full state of the environment s_t at time t is kept hidden from the players. Instead, at time t the agents receive a local observation from the set of joint observations $\Omega = \{\Omega^{(n)}\}_{n \in \mathcal{N}}$, where $\Omega^{(n)}$ is the set of observations for agent n, with transition probability $\mathcal{O}(o_t|s_{t+1}, a_t)$, $\forall o_t \in \Omega$, which is dependent on the hidden environment state after taking a joint action. We treat M_{MDP} as a special case of M_{POMDP} where $o_t^{(n)} = s_t^{(n)}$, that is the observations represent the full environment state information. Hereinafter, all notations will use $o_t^{(n)}$ in place of the local environment state for brevity to encompass all cases.

QMARL is the application of quantum computing to MARL. A popular approach in MARL is through actor-critic architectures, which tune policies, called *actors*, via an estimator for how good or bad the policy is at any given state of an environment, called a *critic*. To do this, the critic needs access to the local agent environment observations to estimate the value for a particular environment state. Current state of the art approaches follow the CTDE framework which deploys the critic on a central server and the actors across decentralized agents. Because the critic and the agents are physically separated, CTDE requires the agents to transmit their local observations to the server for the critic to estimate the joint value, thereby publicizing potentially private local observations. Quantum is often integrated as a drop-in replacement for classical NNs, called VQCs, within many MARL systems. These trainable quantum circuits tune the state of *qubits*, the quantum analog of classical bits, using unitary *gate* operations.

A.2 Quantum computation

A.2.1 Qubit states

A *qubit* is the quantum mechanical analog to the classical bit. The state of a qubit is represented as a 2-dimensional unit vector in complex Hilbert space $\mathcal{H} \in \mathbb{C}^2$. The computational basis is the set of states $\left\{ |0\rangle = \begin{bmatrix} 1 & 0 \end{bmatrix}^T, |1\rangle = \begin{bmatrix} 0 & 1 \end{bmatrix}^T \right\}$ which forms a complete and orthonormal basis in $\mathcal{H}$ (meaning $\langle 0|1\rangle = \langle 1|0\rangle = 0$ and $\langle 0|0\rangle = \langle 1|1\rangle = 1$). All qubit states can be expressed as a linear combination of any complete and orthonormal basis, such as the computational basis, which is called *superposition*. We adopt Dirac notation to describe arbitrary qubit states $|\psi\rangle = \begin{bmatrix} \alpha & \beta \end{bmatrix}^T = \alpha |0\rangle + \beta |1\rangle \in \mathcal{H}$ (called "ket psi") where $|\alpha|^2 + |\beta|^2 = 1$, their conjugate transpose $\langle \psi| = |\psi\rangle^\dagger = \begin{bmatrix} \alpha^* & \beta^* \end{bmatrix} = \alpha^* \langle 0| + \beta^* \langle 1|$ (called "bra psi"), the inner product $\langle \psi_1 | \psi_2 \rangle = \alpha_1^* \alpha_2 + \beta_1^* \beta_2$, and the outer product $|\psi_1\rangle\langle\psi_2| =$

$\begin{bmatrix} \alpha_1\alpha_2^* & \alpha_1\beta_2^* \\ \beta_1\alpha_2^* & \beta_1\beta_2^* \end{bmatrix}$. Quantum systems with D qubits can also be represented by extending the above notation using the Kronecker (tensor) product where $\mathcal{H} = \bigotimes_{d=0}^{D-1} \mathcal{H}_d = (\mathbb{C}^2)^{\otimes D}$ is the complex space of the system state $|\psi\rangle = \bigotimes_{d=0}^{D-1} |\psi_d\rangle$ for all $|\psi_D\rangle \in \mathcal{H}_D$. States that can be represented as either a single ket vector, or a sum of basis states are called *pure* states. For example, $|0\rangle$, $|1\rangle$, and $\frac{1}{\sqrt{2}}(|0\rangle + |1\rangle)$ are all pure states in $\mathcal{H}$.

A.2.2 Quantum gates

A quantum *gate* is an unitary operator (or matrix) U, such that $UU^\dagger = \mathbb{I}$, where $\mathbb{I}$ is the identity matrix, acting on the space $\mathcal{H}$ which maps between qubit states. Here, we use the single-qubit Pauli gates

$$X = \begin{bmatrix} 0 & 1 \\ 1 & 0 \end{bmatrix},\ Y = \begin{bmatrix} 0 & -i \\ i & 0 \end{bmatrix},\ Z = \begin{bmatrix} 1 & 0 \\ 0 & -1 \end{bmatrix}, \tag{A.1}$$

with their parameterized rotations

$$R_X(\theta) = e^{-i\frac{\theta}{2}X},\ R_Y(\theta) = e^{-i\frac{\theta}{2}Y},\ R_Z(\theta) = e^{-i\frac{\theta}{2}Z}, \tag{A.2}$$

where $\theta \in \mathbb{R}[0, 2\pi]$, the Hadamard gate

$$H = \frac{1}{\sqrt{2}} \begin{bmatrix} 1 & 1 \\ 1 & -1 \end{bmatrix}, \tag{A.3}$$

the 2-qubit controlled-X (CX, also called CNOT) gate

$$CX_{1,2} = \text{CNOT}_{1,2} = \begin{bmatrix} \mathbb{I} & \mathbf{0} \\ \mathbf{0} & X \end{bmatrix}, \tag{A.4}$$

and the controlled-Z (CZ) gate

$$CZ_{1,2} = \begin{bmatrix} \mathbb{I} & \mathbf{0} \\ \mathbf{0} & Z \end{bmatrix}, \tag{A.5}$$

which are both controlled by qubit 1 and target qubit 2, where $\mathbf{0}$ is a 2×2 square matrix of zeros.

A.2.3 Entanglement

Consider two arbitrary quantum systems A and B, represented by Hilbert spaces $\mathcal{H}_A$ and $\mathcal{H}_B$. We can represent the Hilbert space of the combined system using the tensor product $\mathcal{H}_A \otimes \mathcal{H}_B$. If the quantum states of the two systems are $|\psi\rangle_A$ and $|\psi\rangle_B$, then the state of the combined system can be represented as $|\psi\rangle_A \otimes |\psi\rangle_B$. Quantum states that can be cleanly represented in this form, i.e., separated by tensor product, are said to be *separable*. Not all quantum states, however, are separable. For example, if we fix a set of basis states $\{|0\rangle_A, |1\rangle_A\} \in \mathcal{H}_A$ and $\{|0\rangle_B, |1\rangle_B\} \in \mathcal{H}_B$, then a general state in the space of $\mathcal{H}_A \otimes \mathcal{H}_B$ can be represented as $|\psi\rangle = \sum_{a\in\{0,1\}} \sum_{b\in\{0,1\}} c_{a,b} |a\rangle_A \otimes |b\rangle_B$, which is separable if there $c_{a,c} = c_a c_b, \forall a, b \in \{0, 1\}$, producing the isolated states $|\psi\rangle_A = \sum_{a\in\{0,1\}} c_a |a\rangle_A$ and $|\psi\rangle_B = \sum_{b\in\{0,1\}} c_b |b\rangle_B$. If, however, there exists one $c_{a,c} \neq c_a c_b$, then the combined state is inseparable. In such cases, if a state is inseparable, it is said to be *entangled*.

The four Bell states $\mathcal{B} = \{|\Phi^+\rangle_{AB}, |\Phi^-\rangle_{AB}, |\Psi^+\rangle_{AB}, |\Psi^-\rangle_{AB}\}$ form a complete basis for two-qubit systems $\mathcal{H}_A \otimes \mathcal{H}_B$, and have the form:

$$\left|\Phi^+\right\rangle_{AB} = \frac{1}{\sqrt{2}} \left(|0\rangle_A |0\rangle_B + |1\rangle_A |1\rangle_B\right), \tag{A.6}$$

$$\left|\Phi^-\right\rangle_{AB} = \frac{1}{\sqrt{2}} \left(|0\rangle_A |0\rangle_B - |1\rangle_A |1\rangle_B\right), \tag{A.7}$$

$$\left|\Psi^+\right\rangle_{AB} = \frac{1}{\sqrt{2}} \left(|0\rangle_A |1\rangle_B + |1\rangle_A |0\rangle_B\right), \tag{A.8}$$

$$\left|\Psi^-\right\rangle_{AB} = \frac{1}{\sqrt{2}} \left(|0\rangle_A |1\rangle_B - |1\rangle_A |0\rangle_B\right). \tag{A.9}$$

Since it is impossible to separate the states of $\mathcal{B}$ into individual systems $\mathcal{H}_A$ and $\mathcal{H}_B$, the four Bell states are entangled. In particular, the Bell states are pure entangled states of the combined system $\mathcal{H}_A \otimes \mathcal{H}_B$, but cannot be separated into pure states of systems $\mathcal{H}_A$ and $\mathcal{H}_B$. Additionally, the four Bell states can be generated by quantum circuits using a combination of Pauli operators with a

constant $|0\rangle_A |0\rangle_B$ input state as follows:

$$\left|\Phi^+\right\rangle_{AB} = \text{CNOT}_{1,2}\left(H \otimes \mathbb{I}\right)|0\rangle_A |0\rangle_B\,, \tag{A.10}$$

$$\left|\Phi^-\right\rangle_{AB} = \text{CNOT}_{1,2}\left(H \otimes \mathbb{I}\right)\left(X \otimes \mathbb{I}\right)|0\rangle_A |0\rangle_B\,, \tag{A.11}$$

$$\left|\Psi^+\right\rangle_{AB} = \text{CNOT}_{1,2}\left(H \otimes \mathbb{I}\right)\left(\mathbb{I} \otimes X\right)|0\rangle_A |0\rangle_B\,, \tag{A.12}$$

$$\left|\Psi^-\right\rangle_{AB} = \text{CNOT}_{1,2}\left(H \otimes \mathbb{I}\right)\left(X \otimes X\right)|0\rangle_A |0\rangle_B \tag{A.13}$$

A.2.4 Projective measurements and observables

A projective measurement is a Hermitian and unitary operator O, such that $O = O^\dagger$ and $OO^\dagger = \mathbb{I}$, called an *observable*. The outcomes of a measurement are defined by an observable's spectral decomposition

$$O = \sum_{m=0}^{M-1} \lambda_m P_m, \tag{A.14}$$

where $M = 2^n$ represents the number of measurement outcomes for n qubits, and m is a specific measurement outcome in terms of eigenvalues λ_m and orthogonal projectors P_m in the respective eigenspace. According to the *Born rule* Born (1926); Logiurato & Smerzi (2012); Masanes et al. (2019), the outcome of measuring an arbitrary state $|\psi\rangle$ will be one of the eigenvalues λ_m, and the state will be projected using the operator $P_m/\sqrt{p(m)}$ with probability:

$$p(m) = \langle\psi| P_m |\psi\rangle = \langle P_m\rangle_\psi \tag{A.15}$$

The expected value of the observable with respect to the arbitrary state $|\psi\rangle$ is given by:

$$\mathbb{E}_\psi[O] = \sum_{m=0}^{M-1} \lambda_m p(m) = \langle O\rangle_\psi \tag{A.16}$$

A.2.5 Commuting Observables

A set of observables $\{O_1, \ldots, O_K\}$ share a common eigenbasis (i.e., a common set of eigenvectors with unique eigenvalues) if

$$[O_i, O_j] = O_i O_j - O_j O_i = 0 \quad \forall i, j \in [1, K] \tag{A.17}$$

i.e., their pair-wise commutator is zero. In such cases the observables in the set are said to be *pair-wise commuting*, which in practice means that all observables in the set can be measured at the same time.

B Joint input entanglement circuits

We use a variation of Bell state entanglement to couple the input qubits of the agent VQC branches. Specifically, we entangle based on the set of four Bell states $\mathcal{B} \in \{\Phi^+, \Phi^-, \Psi^+, \Psi^-\}$, as outlined in (A.10–A.13), using the circuits as shown in Fig. B.1. The circuits in Fig. B.1 generate a quantum state across D qubits, which has the combined Hilbert space $\mathcal{H}^{\otimes D}$. In each of the entangled operators, we select one qubit, q_1, to serve as the master control, and all others, $q_2, \ldots, q_D$, serve as targets. The control qubit functions identically to canonical Bell state entanglement. Here, we extend the gate operations that normally apply to the second qubit, in an $\mathcal{H} \otimes \mathcal{H}$ system, to all qubits in $\mathcal{H}^{\otimes D-1}$. The resulting state is an entangled pure state in $\mathcal{H}^{\otimes D}$.

C Full algorithm

The following algorithm is an expanded version of Algorithm 1, as shown in Algorithm C.1. In Algorithm C.1, we include all operations necessary for training both the agents and the split critic. In eQMARL, there is a set of N quantum agents $\mathcal{N}$ that are physically separated from each other (no cross-agent communication is assumed) and one central quantum server. Each agent $n \in \mathcal{N}$ employs an actor policy network $\pi_{\boldsymbol{\theta}^{(n)}_{\text{actor}}}(a|\boldsymbol{o}^{(n)}_t)$ (which can either classical or quantum in nature) with parameters $\boldsymbol{\theta}^{(n)}_{\text{actor}}$, and a VQC given by (2) with unique parameters $\boldsymbol{\theta}^{(n)}_{\text{critic}}$ and $\boldsymbol{\lambda}^{(n)}$ that serves as one branch in the split critic network. In our experiments we simplify the setup by using policy sharing across the agents, as done in Yun et al. (2023b) and Chen (2023); in other words, $\boldsymbol{\theta}^{(n)}_{\text{actor}} = \boldsymbol{\theta}^{(k)}_{\text{actor}}\ \forall n, k \in \mathcal{N}$. All agents interact with the environment independently and each has its own local data buffer $\mathcal{D}^{(n)}$ populated with local observations, actions, rewards, and next observations

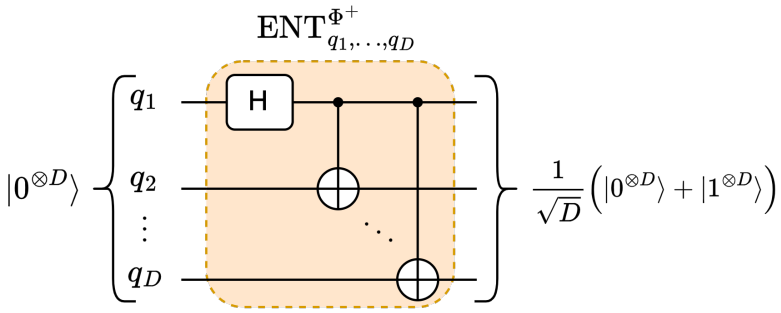

(a) Φ^+

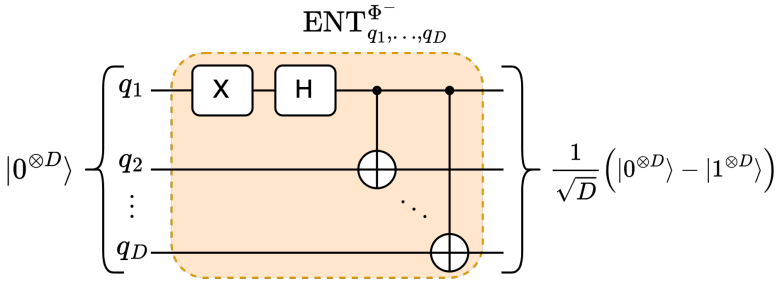

(b) Φ^-

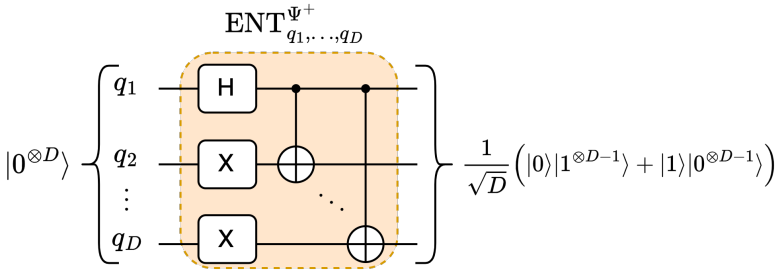

(c) Ψ^+

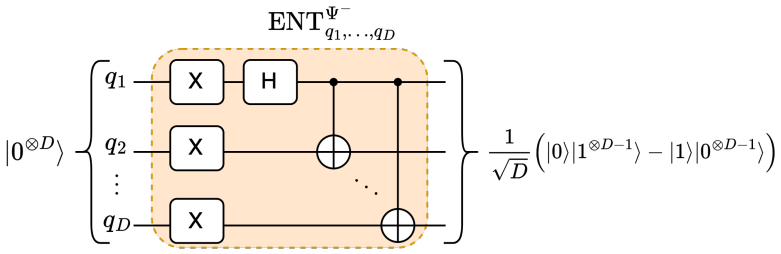

(d) Ψ^-

Figure B.1: Diagrams of joint entanglement operators based on the the four Bell states (a) Φ^+, (b) Φ^-, (c) Ψ^+, (d) Ψ^-.

represented by the 4-tuple $\left(\boldsymbol{o}_t^{(n)}, a_t^{(n)}, r_t^{(n)}, \boldsymbol{o}_{t+1}^{(n)}\right)$ for any instant in time t. These local data are not shared amongst agents, with only the reward and action being communicated classically to the central quantum server (the action only being necessary for policy sharing). Since we employ policy sharing, the final step in eQMARL with this in place is to also estimate the advantage value $A(\boldsymbol{o}_\tau, \boldsymbol{a}_\tau) = Q(\boldsymbol{o}_\tau, \boldsymbol{a}_\tau) - V(\boldsymbol{o}_\tau)$ using the existing value and expected reward estimates, compute actor loss $\mathcal{L}_{\text{actor}}$, compute the gradient of the loss w.r.t the shared actor parameters $\nabla_{\boldsymbol{\theta}_{\text{actor}}}\mathcal{L}_{\text{actor}}$, and

update $\boldsymbol{\theta}_{\text{actor}}$. Note that here we use `Huber` loss for the critic, and for the actors we use entropy-regularized advantage loss. The loss functions are described in detail in Appendix D.

Algorithm C.1: Full eQMARL training using MAA2C for a quantum entangled split critic.

Require: Set of N agents $\mathcal{N}$, 1 quantum entanglement source, and 1 quantum measurement server

Initialize N agent actor networks with shared parameters $\boldsymbol{\theta}_{\text{actor}}$ and local replay buffer $\mathcal{D}^{(n)} = \{\}, \forall n \in \mathcal{N}$;
Initialize N critic branches U_{vqc} with D qubits and parameters $\boldsymbol{\theta}^{(n)}_{\text{critic}}, \boldsymbol{\lambda}^{(n)}, \forall n \in \mathcal{N}$;
for *episode=1, MaxEpisode* **do**
  ▷ `Localized environment interaction.`
  $t = 0$;
  $done = False$;
  while $done \neq True$ *and* $t < max\ steps$ **do**
    for *each agent* $n \in \mathcal{N}$ **do**
      Get local observation $\boldsymbol{o}_t^{(n)}$ from environment;
      Compute $\pi_{\boldsymbol{\theta}^{(n)}_{\text{actor}}}(a|\boldsymbol{o}_t^{(n)})$ and sample $a_t^{(n)}$;
      Apply action $a_t^{(n)}$ and get reward $r_t^{(n)}$ and next observation $\boldsymbol{o}_{t+1}^{(n)}$;
      Update local replay buffer $\mathcal{D}^{(n)} = \mathcal{D}^{(n)} \cup \left\{\left(\boldsymbol{o}_t^{(n)}, a_t^{(n)}, r_t^{(n)}, \boldsymbol{o}_{t+1}^{(n)}\right)\right\}$;
      If $\boldsymbol{o}_{t+1}^{(n)}$ is terminal then communicate $done = True$;
    end
    $t = t + 1$;
  end
  ▷ `eQMARL framework for training.`
  for $\tau \in [0, t-2]$ **do**
    Central quantum server generates $2N$ sets of D entangled qubits and transmits to agents via **quantum channel** (could be prepared a priori and stored in quantum memory);
    for *each agent* $n \in \mathcal{N}$ **do**
      Apply $U_{\text{vqc}}(\boldsymbol{\theta}^{(n)}_{\text{critic}}, \boldsymbol{\lambda}^{(n)}, \boldsymbol{o}_\tau^{(n)})$ and $U_{\text{vqc}}(\boldsymbol{\theta}^{(n)}_{\text{critic}}, \boldsymbol{\lambda}^{(n)}, \boldsymbol{o}_{\tau+1}^{(n)})$ from (2) locally using assigned entangled input qubits;
      Transmit via **quantum channel** the qubits after applying U_{vqc} to central quantum server;
      Transmit via **classical channel** the reward $r_\tau^{(n)}$ and action $a_\tau^{(n)}$ at the current time step to central quantum server (only reward if policy sharing is not used);
    end
    ▷ `Using notation` $\boldsymbol{o}_\tau = \left(\boldsymbol{o}_\tau^{(n)}\right)_{n=1}^N$, $\boldsymbol{o}_{\tau+1} = \left(\boldsymbol{o}_{\tau+1}^{(n)}\right)_{n=1}^N$, $\boldsymbol{a}_\tau = \left(a_\tau^{(n)}\right)_{n=1}^N$.
    Perform joint measurements on qubits across all agents to estimate $V(\boldsymbol{o}_\tau)$ and $V(\boldsymbol{o}_{\tau+1})$ using (3);
    Estimate $Q(\boldsymbol{o}_\tau, \boldsymbol{a}_\tau) = \sum_{n=1}^N r_\tau^{(n)} + \gamma V(\boldsymbol{o}_{\tau+1})$ using discount factor γ;
    Estimate $A(\boldsymbol{o}_\tau, \boldsymbol{a}_\tau) = Q(\boldsymbol{o}_\tau, \boldsymbol{a}_\tau) - V(\boldsymbol{o}_\tau)$ for policy sharing;
    Compute $\nabla_{\boldsymbol{\theta}_{\text{actor}}} \mathcal{L}_{\text{actor}}$ and update $\boldsymbol{\theta}_{\text{actor}}$ for policy sharing;
    Compute $\nabla_{x_{\text{split}}} \mathcal{L}_{\text{critic}}$ and transmit via **classical channel** to each agent to update $\boldsymbol{\theta}^{(n)}_{\text{critic}}$ locally using partial gradient from (4);
  end
end

D LOSS FUNCTIONS

All of our actors and critics are trained using the same loss functions for each experiment. For the critics, we train using `Huber` loss

$$\mathcal{L}_{\text{critic}} = \frac{1}{T-1} \sum_{\tau=0}^{T-1} \begin{cases} \frac{1}{2}(V(\boldsymbol{o}_\tau) - Q(\boldsymbol{o}_\tau, \boldsymbol{a}_\tau))^2 & \text{if } V(\boldsymbol{o}_\tau) - Q(\boldsymbol{o}_\tau, \boldsymbol{a}_\tau) \leq \delta, \\ \delta|V(\boldsymbol{o}_\tau) - Q(\boldsymbol{o}_\tau, \boldsymbol{a}_\tau)| - \frac{1}{2}\delta^2 & \text{otherwise,} \end{cases} \tag{D.1}$$

where δ controls the point in which the loss function turns from quadratic to linear. In this work we use $\delta = 1$. For the actors, we deploy policy sharing amongst the agents. As such, all agents us the same policy parameters, and thus the loss must aggregate the individual losses of each agent. We train using the entropy-regularized advantage function

$$\mathcal{L}_{\text{actor}} = \frac{1}{n(T-1)} \sum_{n=1}^{N} \sum_{\tau=0}^{T-1} \Big[-A(o_\tau^{(n)}, a_\tau^{(n)}) \log_e p(a_\tau^{(n)}) + \alpha H(a_\tau^{(n)}) \Big], \tag{D.2}$$

where
$$H(a_\tau^{(n)}) = -p(a_\tau^{(n)}) \log_e p(a_\tau^{(n)}), \tag{D.3}$$
is the entropy of selecting an action, α controls the influence of entropy, $n \in \mathcal{N}$ is the agent index, and $p(a_\tau^{(n)})$ is the probability of chosen action at time step τ.

E ENVIRONMENT SPECIFICATIONS

E.1 COINGAME

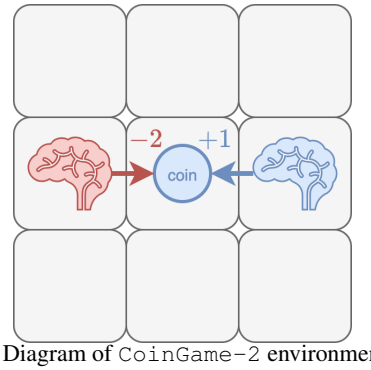

(a) Diagram of `CoinGame-2` environment.

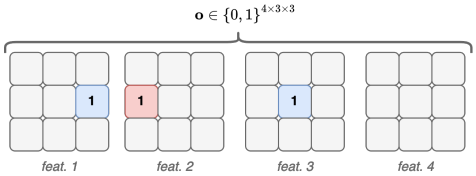

(b) MDP observation dynamics for blue player.

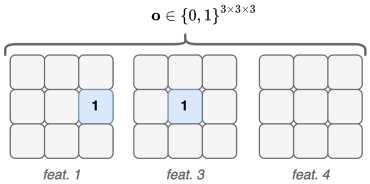

(c) POMDP observation dynamics for blue player.

Figure E.1: Example of (a) `CoinGame-2` environment with two players, colored red and blue, and a single coin colored blue, with visualization of observation matrix for the blue player with (b) MDP dynamics, and (c) POMDP dynamics. Grid squares in (b) and (c) colored grey denote a 0 value, and colored blue/red squares denote a 1 value.

In eQMARL, we train decentralized agents using the `CoinGame-2` environment first proposed in Lerer & Peysakhovich (2018), and as implemented in Phan et al. (2022). The `CoinGame-2` environment pits two agents of different colors (red and blue) on a 3×3 tile grid to collect coins with corresponding color. An example of `CoinGame-2` is shown in Fig. E.1a. Agent observations are a sparse matrix $\mathbf{o}^{(n)} \in \{0,1\}^{4\times3\times3}$ $\forall n \in \mathcal{N}$ with 4 features each with a 3×3 grid world as shown in Fig. E.1b. The features specifically are: 1) A grid with a 1 indicating the agent's location, 2) A grid with a 1 to indicate other agent locations, 3) A grid with a 1 for the location of coins that match the current agent's color, and 4) A grid with a 1 for all other coins (different colors). Since these observations include all information about the game world, the game is considered fully observable and is described by an MDP. We also experiment with a partially observable variant of this game which removes the second feature from agent observations (i.e., the location of other agents), which is a space matrix $\mathbf{o}^{(n)} \in \{0,1\}^{3\times3\times3}$ $\forall n \in \mathcal{N}$. In this partially observed setting, the game is described by a POMDP since agents cannot see each other and thus the full state of the game board is unknown. An example of this observation space is shown in Fig. E.1c. The agents can move along the grid by taking actions in the space $\mathcal{A}^{(n)} = \{\text{north, south, east, west}\}$ $\forall n \in \mathcal{N}$. Each time an agent collects a coin of their corresponding color their episode reward is increased by $+1$, whereas a different color reduces their episode reward by -2. The goal for all agents is to maximize their discounted episode reward. The details of the environment are summarized in Table E.1.

We evaluate agents using three metrics: *score*, *total coins collected*, and *own coin rate*. The *score* metric aggregates all agent undiscounted rewards over a single episode
$$S = \sum_{n=1}^{N} \sum_{t=0}^{T-1} r_t^{(n)} \tag{E.1}$$
where $n \in \mathcal{N}$ is the agent index, $t \in [0, T-1]$ is the episode time index, T is the episode time limit, and $r_t^{(n)}$ is the undiscounted agent reward at time t. The *total coins collected* metric gives insight into how active the agents were during the game
$$TC = \sum_{n=1}^{N} \sum_{t=0}^{T-1} c_t^{(n)} \tag{E.2}$$
where $c_t^{(n)}$ is the total number of coins collected by agent n at time t. Finally, the *own coin rate* metric gives insight into how the agents achieve cooperation, specifically by being selective on which

Table E.1: Specifications for `CoinGame-2` environment with *MDP* and *POMDP* dynamics.

Parameter	Value
Observation for agent n at time t	• MDP: $\boldsymbol{o}_t^{(n)} \in \{0,1\}^{4\times3\times3}$ (dimension is 36) • POMDP: $\boldsymbol{o}_t^{(n)} \in \{0,1\}^{3\times3\times3}$ (dimension is 27)
Number of players (N)	2
Time limit (T)	50
Action for agent n at time t	$a_t^{(n)} \in \{\text{north}, \text{south}, \text{east}, \text{west}\}$
Reward for agent n at time t	$r_t^{(n)} = \begin{cases} +1, & \text{if agent } n \text{ collects coin of same color,} \\ -2, & \text{if agent } n \text{ collects coin of different color,} \\ 0, & \text{otherwise} \end{cases}$
Discount factor (γ)	0.99
Entropy coefficient (α)	0.001

coins they procure

$$OCR = \sum_{n=1}^{N} \sum_{t=0}^{T-1} k_t^{(n)} / c_t^{(n)} \tag{E.3}$$

where $k_t^{(n)}$ is the number of coins collected of the corresponding agent's color.

E.2 CartPole

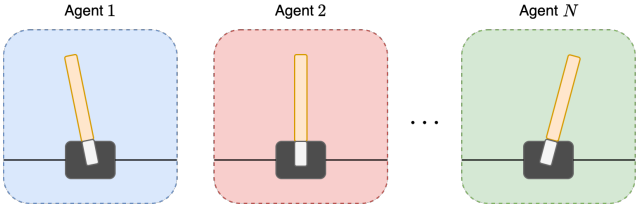

Figure E.2: Example of an N-agent `CartPole` environment colored red, blue, and green.

We also train eQMARL using a multi-agent variant of the `CartPole` environment as proposed in Barto et al. (1983). The multi-agent `CartPole` environment runs multiple independent instances of the single-agent variant in parallel. This environment setup is an interesting case study for multi-agent learning because the observations of each agent are completely independent from one another; that is, observations from sibling environments are not strictly necessary to develop a strategy for a specific environment instance. This allows us to examine the impacts of both explicit and implicit cooperation between independent agents. An example of `CartPole` with N agents is shown in Fig. E.2. Agent observations are a matrix $\mathbf{o}^{(n)} \in \mathbb{R}^{4\times1}$ $\forall n \in \mathcal{N}$ with 4 real-valued features. The features are: 1) Cart position with range $[-4.8, 4.8]$, 2) Cart velocity with range $(-\infty, \infty)$, 3) Pole angle in *radians* with range $[-0.418, 0.418]$, and 4) Pole angular velocity with range $(-\infty, \infty)$. The pole is considered *balanced* if the pole angle feature stays within the range $[-.2095, .2095]$ radians, and the cart position feature stays within the range $[-2.4, 2.4]$. These observations include all information about the environment, and thus the environment under these conditions is considered *fully observable* and described by an MDP. We also consider a *partially observed* variant of the environment which removes the second feature from agent observations (i.e., the cart velocity), which is a matrix $\mathbf{o}^{(n)} \in \mathbb{R}^{3\times1}$ $\forall n \in \mathcal{N}$. The environment is described by a POMDP in this setting since agents are unaware of their cart's velocity, and thus the full state of the environment is unknown. Notably, in this multi-agent variant of the environment the agent observations in both settings are independent from each other. The agents interact with the environment by taking actions in the space $\mathcal{A}^{(n)} = \{\text{left}, \text{right}\}$ $\forall n \in \mathcal{N}$, which correspond to pushing their cart to the left and right respectively. Similar to the observations, the agent actions are also independent and do not affect neighboring environments. Each time step an agent is successful in keeping their pole balanced they receive a $+1$ episode reward. The episode terminates when an observation falls outside of the balanced range. The goal for all agents is to maximize their expected total episode reward (i.e., the number of time steps they are able to keep the pole balanced). The details of the environment are summarized in Table E.2.

Table E.2: Specifications for multi-agent `CartPole` environment with *MDP* and *POMDP* dynamics.

Parameter	Value
Observation for agent n at time t	• MDP: $\boldsymbol{o}_t^{(n)} \in \mathbb{R}^{4\times 1}$ • POMDP: $\boldsymbol{o}_t^{(n)} \in \mathbb{R}^{3\times 1}$
Number of players (N)	2
Time limit (T)	500
Action for agent n at time t	$a_t^{(n)} \in \{\text{left}, \text{right}\}$
Reward for agent n at time t	$r_t^{(n)} = \begin{cases} +1, & \text{if pole for agent } n \text{ is balanced,} \\ 0, & \text{otherwise} \end{cases}$

We evaluate the agents using the *average reward* metric, which aggregates all agent rewards over a single episode

$$AR = \frac{1}{N}\sum_{n=1}^{N}\sum_{t=0}^{T-1} r_t^{(n)} \tag{E.4}$$

where $n \in \mathcal{N}$ is the agent index, $t \in [0, T-1]$ is the episode time index, T is the episode time limit, and $r_t^{(n)}$ is the agent reward at time t.

F Quantum encoding transformations

To encode environment observations into our quantum models we first apply a transformation on the observation matrix. This allows us to reduce its dimensions, thereby making it usable for the limited number of qubits available to NISQ systems, while also changing the range of matrix values to be suitable for input into one of the Pauli rotation gates.

F.1 `CoinGame-2` Environment

MDP dynamics For the `CoinGame-2` environment with fully observed state dynamics we use the transformation

$$f_{\text{MDP}}(\mathbf{o}_{i\times j\times k}) = \sum_k \mathbf{o}_{i\times j,k} 2^{-k} \tag{F.1}$$

which sums over the last dimension of the observation matrix $\mathbf{o}_{i\times j\times k}$ with shape $i \times j \times k$. In the case of `CoinGame-2` with MDP dynamics the observations have shape $4 \times 3 \times 3$. This transformation reduces the dimensions to $4 \times 3 \times 1$, which can be directly fed into the encoder architecture outlined in Section 2.2.

POMDP dynamics For the `CoinGame-2` environment with partially observed state dynamics our quantum models employ a small classical NN at the input of the encoder for dimensionality reduction, as done in Chen (2023). In particular, we use the transformation

$$f_{\text{POMDP}}(\mathbf{o}_{i\times j\times k}) = \mathbf{w}_{ijk\times 3d} \cdot \text{flatten}(\mathbf{o}_{i\times j\times k})^T + b \tag{F.2}$$

which flattens the observation matrix $\mathbf{o}_{i\times j\times k}$ with shape $i \times j \times k$ and passes it through a single fully-connected NN layer with parameters $\mathbf{w}_{ijk\times 3d}$ and b, and d is the number of qubits. Note that, in POMDP, the trainable quantum encoding parameters $\boldsymbol{\lambda}^{(n)}$ are no longer necessary. In this case, we set $\boldsymbol{\lambda}^{(n)} = \mathbf{1}$, where $\mathbf{1}$ is a matrix of ones.

F.2 `CartPole` Environment

Observation scaling For the `CartPole` environment we apply a constant observation scaling to both MDP and POMDP dynamics to normalize their values. In particular, we use the transformation

$$f(\mathbf{o}_{i\times j}) = \mathbf{o}_{i\times j}/\mathbf{v}_i \tag{F.3}$$

where

$$\mathbf{v} = [2.4, 2.5, 0.21, 2.5]^\intercal \tag{F.4}$$

is a constant scaling vector.

POMDP dynamics For the `CartPole` environment with partially observed state dynamics we apply an additional transformation similar to the `CoinGame-2` POMDP case to reduce input feature dimensions. In particular, we apply the transformation,

$$f_{\text{POMDP}}(\mathbf{o}_{i\times j}) = \mathbf{w}_{ij\times 3d} \cdot \text{flatten}(\mathbf{o}_{i\times j})^T + b \tag{F.5}$$

which flattens the observation matrix $\mathbf{o}_{i\times j}$ with shape $i \times j$ and passes it through a single fully-connected NN layer with parameters $\mathbf{w}_{ij\times 3d}$ and b, and d is the number of qubits.

G MODEL HYPERPARAMETERS

The hyperparameters for each of the models trained in our experiments, as discussed in Section 3.2, are shown in Tables G.1 and G.2. Table G.1 shows the parameters for the quantum models, as used in qfCTDE and eQMARL. Table G.2 shows the paramters for the classical models, as used in fCTDE and sCTDE.

Table G.1: Hyperparameters for both qfCTDE and eQMARL, actor and critic, used on both the `CoinGame-2` and multi-agent `CartPole` environments with MDP and POMDP dynamics.

Parameter	Value
NN encoder transform activation	• MDP: N/A • POMDP: linear
Flag $\boldsymbol{\lambda}^{(n)}$ as trainable	• MDP: True • POMDP: False
Number of qubits per agent (D)	4
(eQMARL only) Input entanglement type (B) for critic	Ψ^+
Number of layers (L) in U_{vqc}	5
Squash activation (ϕ)	arctan
Inverse temperature (β)	1
Optimizer	Adam
Learning rate	$[0.01, 0.1, 0.1]$

Table G.2: Hyperparameters for both fCTDE and sCTDE, actor and critic, used on both the `CoinGame-2` and multi-agent `CartPole` environments with MDP and POMDP dynamics.

Parameter	Value
NN hidden units (h)	$[12]$
Optimizer	Adam
Learning rate	0.001

H EXPERIMENT RESULTS

H.1 ENTANGLEMENT STYLE COMPARISON

The empirical results for the entanglement comparison experiment, as discussed in Section 3.3, are shown in Tables H.1 and H.2. Table H.1 shows the score metric statistics mean, standard deviation, and 95% confidence interval for each of the entanglement styles Ψ^+, Ψ^-, Φ^+, Φ^-, and `None`. Table H.2 shows the convergence time, in epochs, to each of the score thresholds 20, 25, and also to the maximum score value (reported parenthetically in *italics*) for each of the entanglement styles. The best values in each column are highlighted in **bold**.

Fig. H.1 shows the training results for the entanglement styles as discussed in Section 3.3. In particular, we provide the full set of performance metrics of score, total coins collected, own coins collected, and own coin rate, as outlined in Appendix E, (E.1–E.3). Fig. H.1 shows the results for the entanglement styles Ψ^+, Ψ^-, Φ^+, Φ^-, and `None`, as discussed in Section 3.3. The left column, Figs. H.1a, H.1c, H.1e, and H.1g, shows the performance for MDP environment dynamics. Similarly, the right column, Figs. H.1b, H.1d, H.1f, and H.1h, shows the performance for POMDP environment dynamics.

Table H.1: Comparison of entanglement style score performance for MDP and POMDP `CoinGame-2` environment dynamics using mean, standard deviation, and 95% confidence interval statistics. Best values are highlighted in bold.

		Score		
Dynamics	Entanglement	Mean	SD	95% CI
MDP	Ψ^+	**21.11**	2.65	(20.92, 21.29)
	Ψ^-	20.85	2.70	(20.61, 21.07)
	Φ^+	21.02	**2.54**	(20.77, 21.30)
	Φ^-	20.43	3.85	(20.20, 20.59)
	`None`	20.00	3.80	(19.75, 20.20)
POMDP	Ψ^+	18.49	**3.91**	(18.15, 18.74)
	Ψ^-	17.77	4.05	(17.40, 18.09)
	Φ^+	17.01	6.28	(16.74, 17.25)
	Φ^-	14.73	7.63	(14.45, 15.01)
	`None`	**18.57**	4.26	(18.28, 18.82)

Table H.2: Comparison of entanglement style score convergence (in number of epochs) for MDP and POMDP `CoinGame-2` environment dynamics. Best values are highlighted in bold.

		Epochs to Score Threshold		
Dynamics	Entanglement	20	25	Max (*value*)
MDP	Ψ^+	**568**	2332	2942 (***25.67***)
	Ψ^-	595	1987	2849 (*25.45*)
	Φ^+	612	**1883**	2851 (*25.51*)
	Φ^-	691	2378	2984 (*25.23*)
	`None`	839	2337	**2495** (*25.12*)
POMDP	Ψ^+	**1049**	**1745**	2950 (*26.28*)
	Ψ^-	1206	2114	2999 (*25.95*)
	Φ^+	1269	-	2992 (*24.1*)
	Φ^-	1838	-	2727 (*22.8*)
	`None`	1069	1955	**2841** (***26.39***)

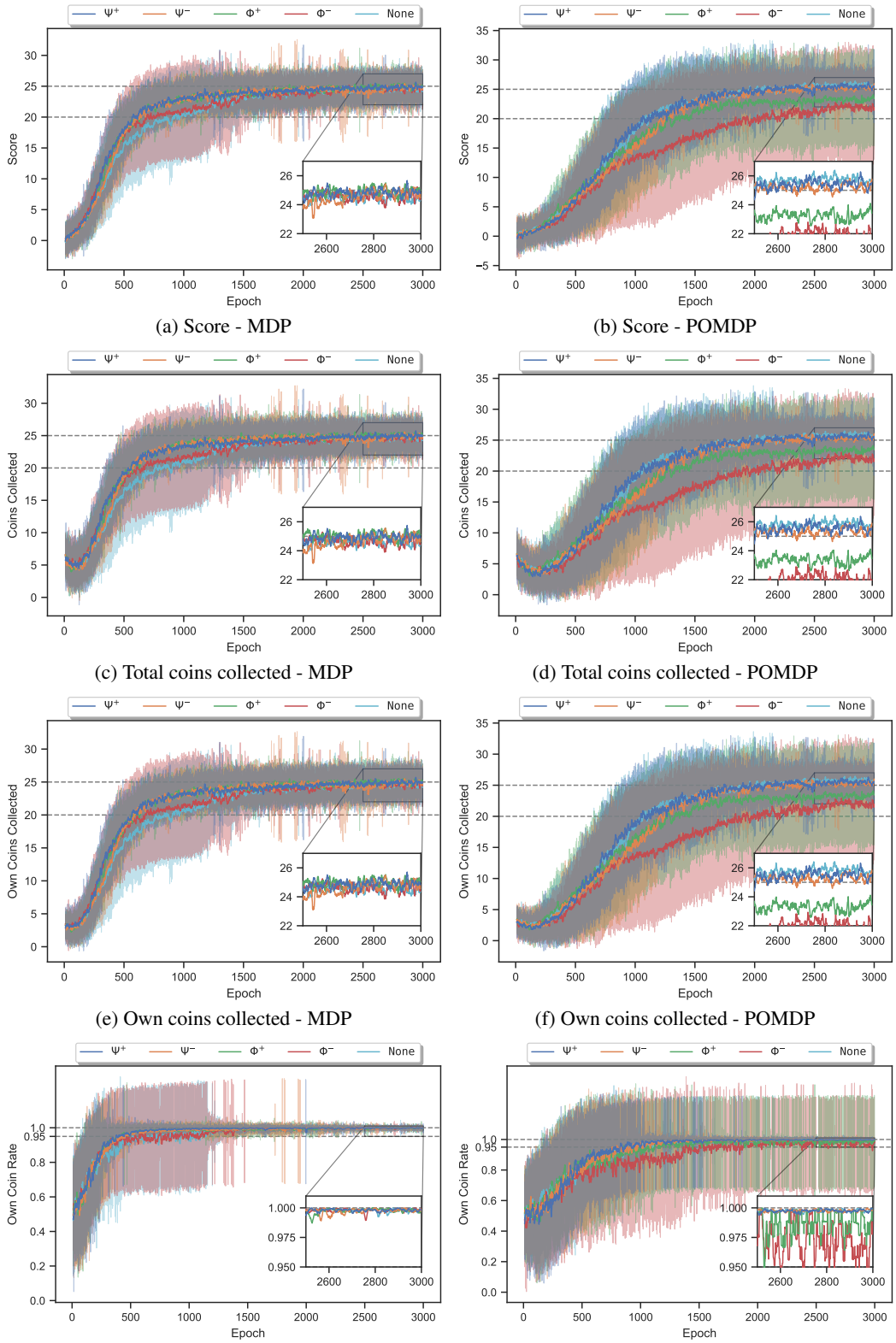

(a) Score - MDP

(b) Score - POMDP

(c) Total coins collected - MDP

(d) Total coins collected - POMDP

(e) Own coins collected - MDP

(f) Own coins collected - POMDP

(g) Own coin rate - MDP

(h) Own coin rate - POMDP

Figure H.1: Comparison of `CoinGame-2` MDP and POMDP environment performance metrics (a,b) score, (c,d) total coins collected, (e,f) own coins collected, and (g,h) own coin rate for eQMARL with varying input quantum entanglement styles Ψ^+ (blue), Ψ^- (orange), Φ^+ (green), Φ^- (red), and `None` (cyan) averaged over 10 runs, with ± 1 std. dev. shown as shaded regions.

H.2 CoinGame BASELINES COMPARISON

The empirical results for eQMARL-Ψ^+, qfCTDE, fCTDE, and sCTDE, as discussed in Section 3.4, are shown in Tables H.2 and H.4 and Fig. H.2. The performance for MDP dynamics is shown in Figs. H.2a, H.2c, H.2e, and H.2g, and for POMDP dynamics is shown in Figs. H.2b, H.2d, H.2f, and H.2h. Importantly, Fig. H.2 shed light on when, and how, a cooperative strategy is achieved by each framework. Further, through Fig. H.2 we also observe the relationship between the metrics outlined in Appendix E.1. This connection is important, as a single metric in isolation only paints part of the performance picture. A full comparison can be achieved by considering the metrics as as group, and, particularly, the relationship between agent score, i.e., the sum of rewards, and own coin rate, i.e., the priority given to coins of matching color.

Table H.3: Comparison of model score and own coin rate performance for MDP and POMDP CoinGame-2 environment dynamics using mean, standard deviation, and 95% confidence interval statistics. Best values are highlighted in bold.

		Score			Own Coin Rate		
Dynamics	Framework	Mean	SD	95% CI	Mean	SD	95% CI
MDP	eQMARL-Ψ^+	**21.11**	**2.65**	**(20.91, 21.37)**	**0.9640**	**0.0347**	**(0.9606, 0.9667)**
	qfCTDE	19.41	6.23	(19.22, 19.60)	0.9398	0.1020	(0.9367, 0.9423)
	sCTDE	14.18	2.69	(13.87, 14.53)	0.8504	0.0928	(0.8436, 0.8558)
	fCTDE	12.36	4.41	(12.01, 12.66)	0.8202	0.1379	(0.8153, 0.8255)
POMDP	eQMARL-Ψ^+	**18.49**	3.91	**(18.24, 18.75)**	**0.9226**	**0.0831**	**(0.9173, 0.9281)**
	qfCTDE	16.79	4.66	(16.43, 17.19)	0.9040	0.1135	(0.8991, 0.9094)
	sCTDE	13.70	**2.79**	(13.33, 14.07)	0.8466	0.0985	(0.8407, 0.8525)
	fCTDE	13.46	3.24	(13.08, 13.75)	0.8443	0.1026	(0.8389, 0.8495)

Table H.4: Comparison of model score and own coin rate convergence (in number of epochs) for MDP and POMDP CoinGame-2 environment dynamics. Best values are highlighted in bold.

		Epochs to Score Threshold			Epochs to Own Coin Rate Threshold		
Dynamics	Framework	20	25	Max (*value*)	0.95	1.0	Max (*value*)
MDP	eQMARL-Ψ^+	**568**	**2332**	2942 (***25.67***)	**376**	**2136**	**2136** (***1.0***)
	qfCTDE	678	-	**2378** (*23.38*)	397	-	2832 (*0.9972*)
	sCTDE	1640	2615	2631 (*25.3*)	1511	-	2637 (*0.9864*)
	fCTDE	1917	-	2925 (*23.67*)	1700	-	2909 (*0.9857*)
POMDP	eQMARL-Ψ^+	**1049**	**1745**	2950 (***26.28***)	**773**	-	**2533** (*0.9997*)
	qfCTDE	1382	2124	2871 (*26.09*)	1038	**2887**	2887 (***1.0***)
	sCTDE	1738	2750	2999 (*25.33*)	1588	-	2956 (*0.9894*)
	fCTDE	1798	2658	**2824** (*25.49*)	1574	-	2963 (*0.9894*)

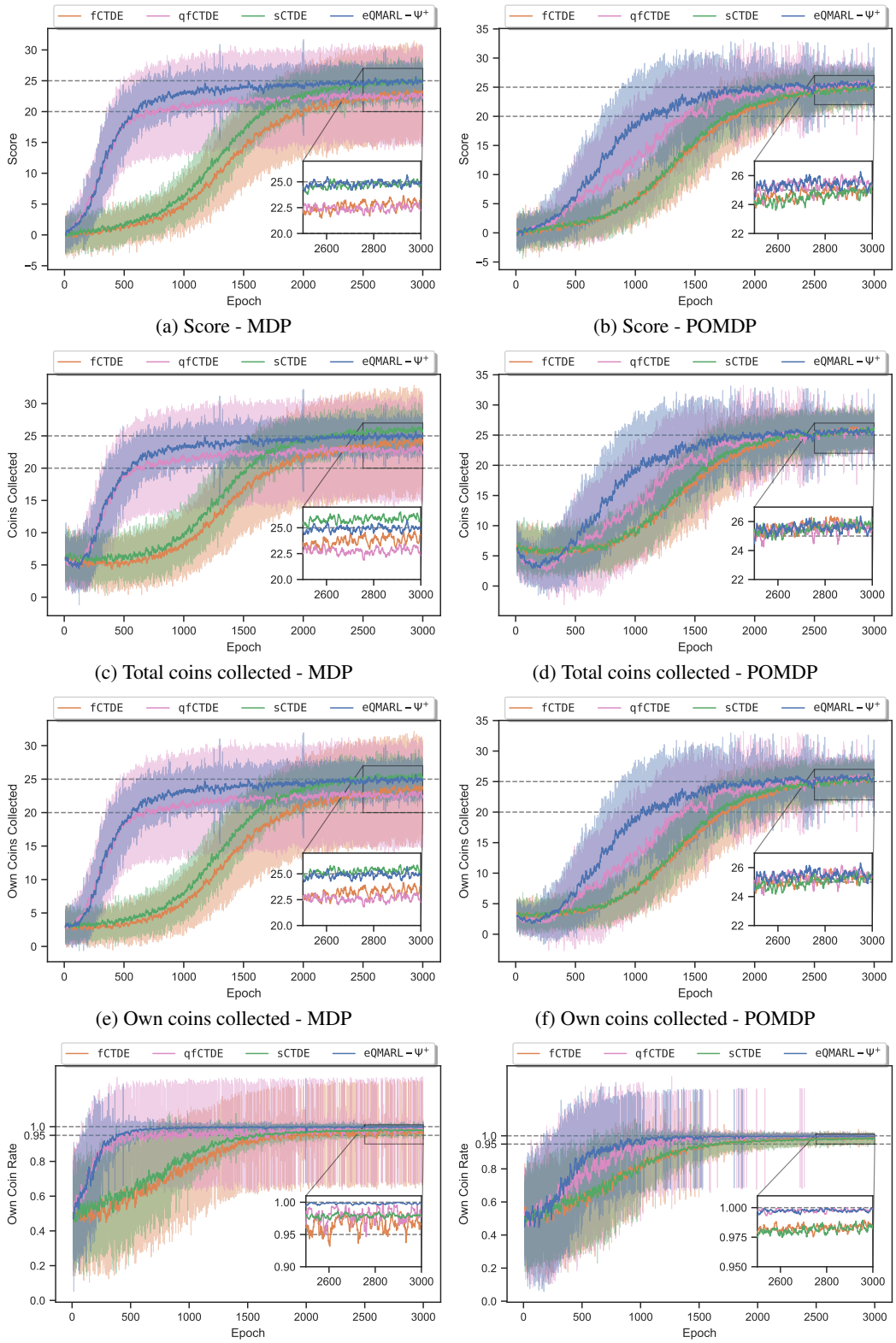

(a) Score - MDP

(b) Score - POMDP

(c) Total coins collected - MDP

(d) Total coins collected - POMDP

(e) Own coins collected - MDP

(f) Own coins collected - POMDP

(g) Own coin rate - MDP

(h) Own coin rate - POMDP

Figure H.2: Comparison of `CoinGame-2` MDP and POMDP environment performance metrics (a,b) score, (c,d) total coins collected, (e,f) own coins collected, and (g,h) own coin rate for `fCTDE` (orange), `qfCTDE` (magenta), `sCTDE` (green), and `eQMARL-`Ψ^+ (blue) averaged over 10 runs, with ± 1 std. dev. shown as shaded regions.

H.3 CartPole BASELINES COMPARISON

The empirical results for eQMARL-Ψ^+, qfCTDE, fCTDE, and sCTDE, as discussed in Section 3.5, are shown in Tables H.5 and H.6 and Fig. H.3. The performance for MDP dynamics is shown in Fig. H.3a, and for POMDP dynamics is shown in Fig. H.3b. Importantly, from this we see that the classical models do not perform well overall in either setting, and qfCTDE experiences high variance in the MDP case. Even though sCTDE has a higher reward at the end of training in the POMDP case, it converges considerably more slowly, experiencing high variance at the end, and requires over 400 more epochs achieve a mean value less than half of eQMARL. In contrast, eQMARL is more stable than qfCTDE, and more rapidly converges to a higher mean reward than fCTDE and sCTDE across both settings.

Table H.5: Comparison of model average reward performance for MDP and POMDP CartPole environment dynamics using mean, standard deviation, and 95% confidence interval statistics.

		Reward		
Dynamics	Framework	Mean	SD	95% CI
MDP	eQMARL-Ψ^+	79.11	50.62	(77.26, 81.01)
	qfCTDE	121.35	110.13	(117.95, 124.59)
	sCTDE	16.07	22.15	(15.90, 16.21)
	fCTDE	15.14	17.43	(15.06, 15.22)
POMDP	eQMARL-Ψ^+	82.28	44.24	(80.80, 83.91)
	qfCTDE	79.03	44.06	(76.27, 81.02)
	sCTDE	47.59	29.71	(44.71, 50.86)
	fCTDE	11.62	32.02	(11.45, 11.82)

Table H.6: Comparison of model average reward convergence (in number of epochs) for MDP and POMDP CartPole environment dynamics.

		Epochs to Average Reward Threshold	
Dynamics	Framework	Mean (*value*)	Max (*value*)
MDP	eQMARL-Ψ^+	166 (*79.11*)	555 (*134.16*)
	qfCTDE	189 (121.35)	810 (*262.43*)
	sCTDE	23 (*16.07*)	978 (*24.64*)
	fCTDE	9 (*15.14*)	44 (*19.43*)
POMDP	eQMARL-Ψ^+	251 (*82.28*)	770 (*127.60*)
	qfCTDE	276 (*79.03*)	648 (*137.66*)
	sCTDE	669 (*47.59*)	998 (*172.16*)
	fCTDE	9 (*11.62*)	999 (*28.83*)

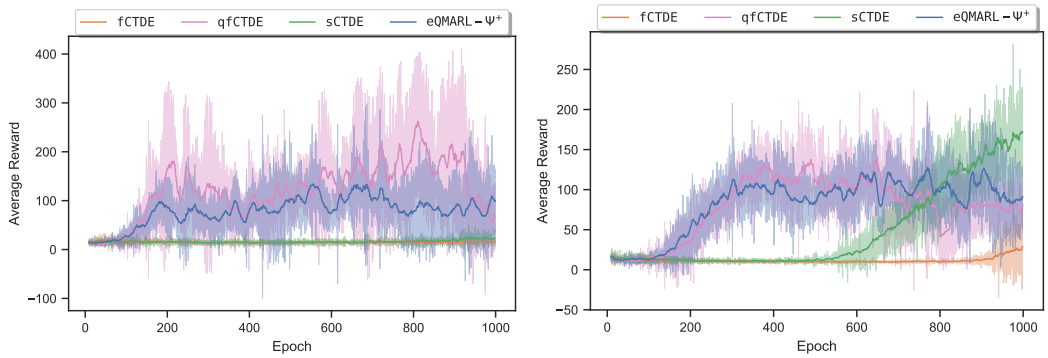

(a) Average Reward - MDP (b) Average Reward - POMDP

Figure H.3: Comparison of CartPole MDP and POMDP environment average reward performance for fCTDE (orange), qfCTDE (magenta), sCTDE (green), and eQMARL-Ψ^+ (blue) averaged over 5 runs of 1000 epochs, with ± 1 std. dev. shown as shaded regions.

H.4 Ablation Study

The empirical results for the ablation study as discussed in Section 3.6 are shown in Table H.7 and Figs. H.4 and H.5. Looking at the statistics in Table H.7 and the convergence in Figs. H.4 and H.5, we can see that our selection of $h = 12$ hidden units for the baselines and $L = 5$ for the quantum models is fair because of the significant performance drops and increased variation incurred by reducing, and the limited gains by increasing, the number of units and layers. This choice for architecture results in the most comparable performance across all baselines. From the results of this ablation study, we can more concretely represent a comparison of the final sizes of the actor and critic models, in number of trainable parameters, for `eQMARL`, `qfCTDE`, `fCTDE`, and `sCTDE`. The final selected model sizes, in number of trainable parameters, are shown in Table H.8.

Table H.7: Ablation study with classical model hidden layer units $h \in \{3, 6, 12, 24\}$ and quantum VQC layers $L \in \{2, 5, 10\}$. Compares model size in number of trainable critic parameters with score and own coin rate performance for MDP and POMDP `CoinGame-2` environment dynamics using mean, standard deviation, and 95% confidence interval statistics.

			Score			Own Coin Rate		
Dynamics	Framework	Params	Mean	SD	95% CI	Mean	SD	95% CI
MDP	`fCTDE-3`	223	2.42	2.35	(2.35, 2.49)	0.6720	0.2024	(0.6685, 0.6769)
	`fCTDE-6`	445	7.41	3.46	(7.19, 7.65)	0.7658	0.1414	(0.7610, 0.7712)
	`fCTDE-12`	889	12.36	4.41	(12.09, 12.67)	0.8202	0.1379	(0.8139, 0.8262)
	`fCTDE-24`	1777	17.63	2.58	(17.25, 17.91)	0.8823	0.0751	(0.8770, 0.8875)
	`sCTDE-3`	229	3.24	3.09	(3.16, 3.33)	0.6852	0.1991	(0.6821, 0.6897)
	`sCTDE-6`	457	8.54	3.67	(8.29, 8.78)	0.7857	0.1327	(0.7804, 0.7924)
	`sCTDE-12`	913	14.18	2.69	(13.90, 14.60)	0.8504	0.0928	(0.8454, 0.8553)
	`sCTDE-24`	1825	18.18	2.41	(17.84, 18.53)	0.8936	0.0673	(0.8896, 0.8979)
	`qfCTDE-L2`	121	6.58	3.92	(6.47, 6.66)	0.8482	0.1921	(0.8435, 0.8518)
	`qfCTDE-L5`	265	19.41	6.23	(19.23, 19.59)	0.9398	0.1020	(0.9366, 0.9426)
	`qfCTDE-L10`	505	22.08	2.22	(21.91, 22.26)	0.9691	0.0247	(0.9665, 0.9723)
	`eQMARL-`Ψ^+`-L2`	121	5.38	3.74	(5.30, 5.46)	0.8271	0.2213	(0.8234, 0.8300)
	`eQMARL-`Ψ^+`-L5`	265	21.11	2.65	(20.92, 21.35)	0.9640	0.0347	(0.9601, 0.9667)
	`eQMARL-`Ψ^+`-L10`	505	22.45	2.23	(22.28, 22.62)	0.9719	0.0219	(0.9685, 0.9745)
POMDP	`fCTDE-3`	169	2.98	2.47	(2.91, 3.05)	0.7082	0.1890	(0.7039, 0.7123)
	`fCTDE-6`	337	7.15	3.06	(6.95, 7.37)	0.7711	0.1388	(0.7658, 0.7781)
	`fCTDE-12`	673	13.46	3.24	(13.09, 13.76)	0.8443	0.1026	(0.8396, 0.8506)
	`fCTDE-24`	1345	17.38	2.65	(17.06, 17.73)	0.8889	0.0752	(0.8840, 0.8945)
	`sCTDE-3`	175	2.68	2.60	(2.61, 2.74)	0.6834	0.1942	(0.6792, 0.6866)
	`sCTDE-6`	349	6.35	3.53	(6.18, 6.54)	0.7677	0.1488	(0.7633, 0.7725)
	`sCTDE-12`	697	13.70	2.79	(13.44, 13.99)	0.8466	0.0985	(0.8411, 0.8515)
	`sCTDE-24`	1393	17.97	2.60	(17.67, 18.25)	0.8948	0.0723	(0.8898, 0.9004)
	`qfCTDE-L2`	745	12.34	7.56	(12.09, 12.60)	0.8335	0.2058	(0.8277, 0.8386)
	`qfCTDE-L5`	817	16.79	4.66	(16.45, 17.04)	0.9040	0.1135	(0.8994, 0.9091)
	`qfCTDE-L10`	937	18.14	4.28	(17.83, 18.31)	0.9476	0.0660	(0.9443, 0.9508)
	`eQMARL-`Ψ^+`-L2`	745	17.14	3.98	(16.77, 17.47)	0.8834	0.1106	(0.8769, 0.8896)
	`eQMARL-`Ψ^+`-L5`	817	18.49	3.91	(18.23, 18.80)	0.9226	0.0831	(0.9172, 0.9272)
	`eQMARL-`Ψ^+`-L10`	937	19.09	3.44	(18.86, 19.46)	0.9485	0.0603	(0.9458, 0.9523)

Table H.8: Comparison of the best model size in number of trainable parameters for each framework used on `CoinGame-2` environment with *MDP* and *POMDP* dynamics.

			Number of Trainable Parameters	
Framework	Ablation Selection	Model	*MDP dynamics*	*POMDP dynamics*
`eQMARL`	$L = 5$	Actor	136	412
	$L = 5$	Critic	265 (132 per agent, 1 central)	817 (408 per agent, 1 central)
`qfCTDE`	$L = 5$	Actor	136	412
	$L = 5$	Critic	265	817
`fCTDE`	$h = 12$	Actor	496	388
	$h = 12$	Critic	889	673
`sCTDE`	$h = 12$	Actor	496	388
	$h = 12$	Critic	913 (444 per agent, 25 central)	697 (336 per agent, 25 central)

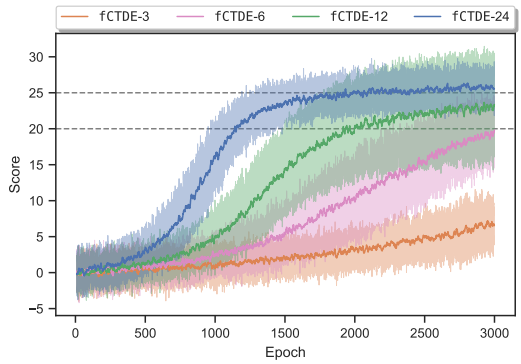

(a) fCTDE - MDP - Score

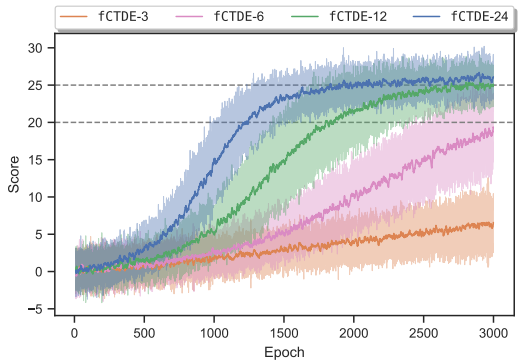

(b) fCTDE - POMDP - Score

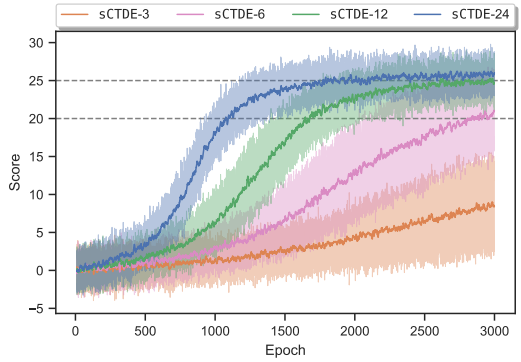

(c) sCTDE - MDP - Score

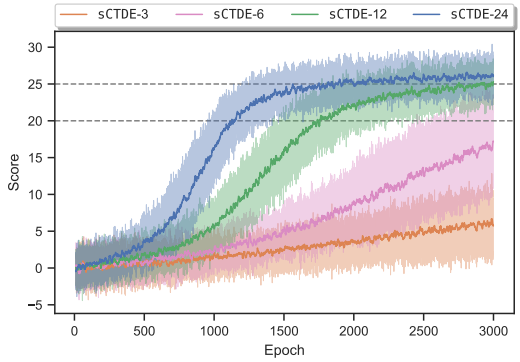

(d) sCTDE - POMDP - Score

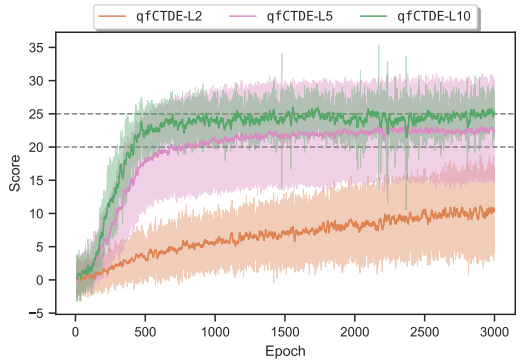

(e) qfCTDE - MDP - Score

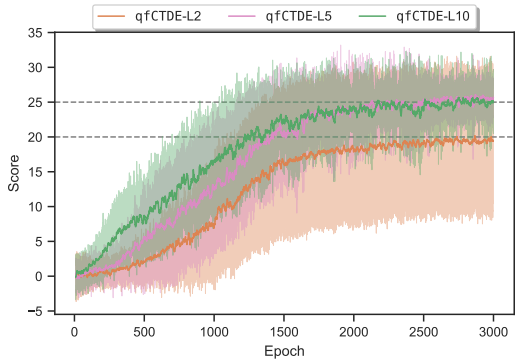

(f) qfCTDE - POMDP - Score

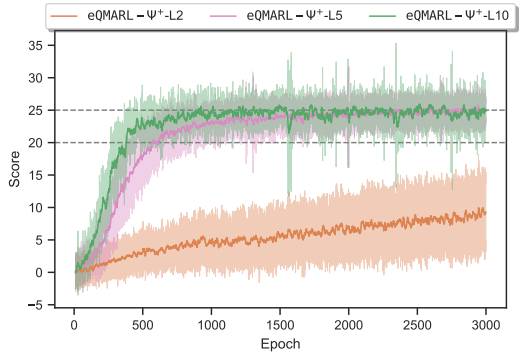

(g) eQMARL-Ψ^+ - MDP - Score

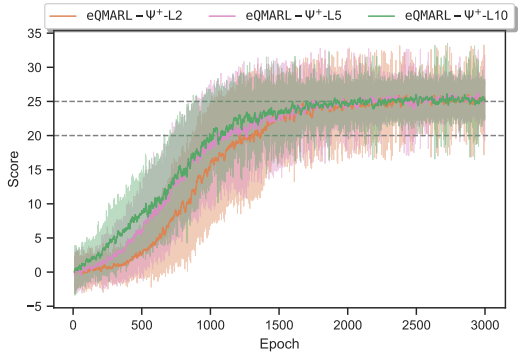

(h) eQMARL-Ψ^+ - POMDP - Score

Figure H.4: Score performance for ablation study using `CoinGame-2` for (a,b) fCTDE, and (c,d) sCTDE, and (e,f) qfCTDE, and (g,h) eQMARL-Ψ^+ with hidden layer units $h \in \{3, 6, 12, 24\}$ and VQC layers $L \in \{2, 5, 10\}$, averaged over 10 runs of 3000 epochs, with ± 1 std. dev. shown as shaded regions.

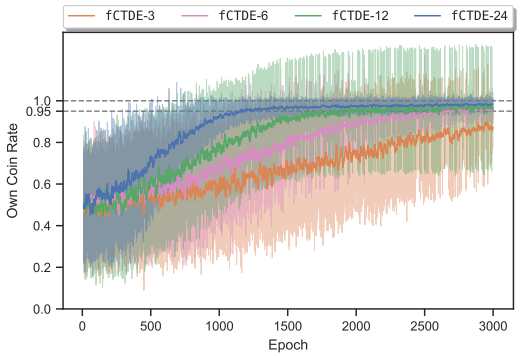

(a) fCTDE - MDP - Own Own Coin Rate

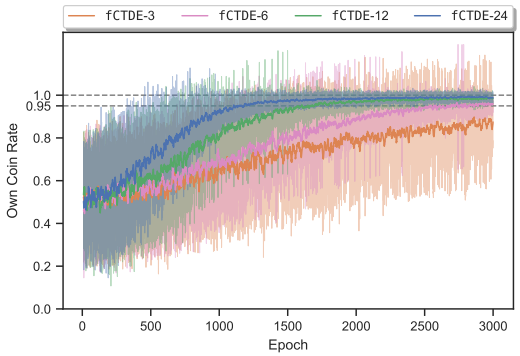

(b) fCTDE - POMDP - Own Coin Rate

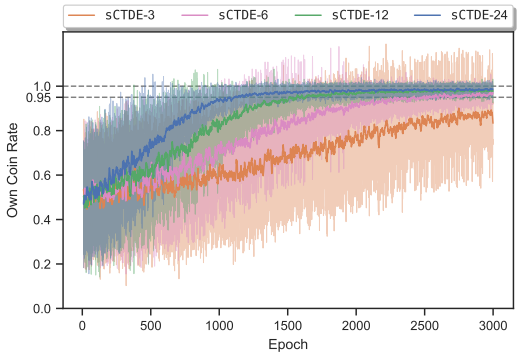

(c) sCTDE - MDP - Own Own Coin Rate

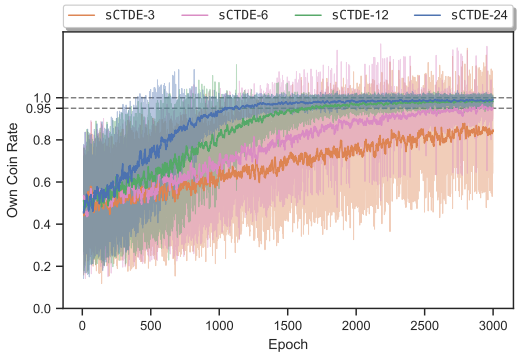

(d) sCTDE - POMDP - Own Own Coin Rate

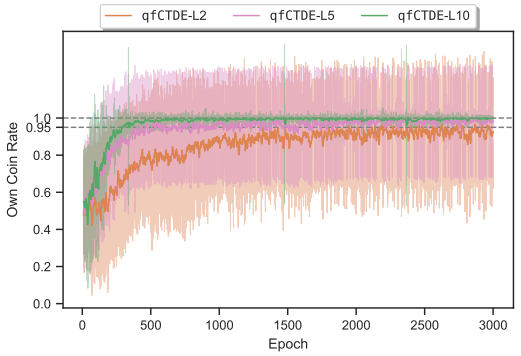

(e) qfCTDE - MDP - Own Own Coin Rate

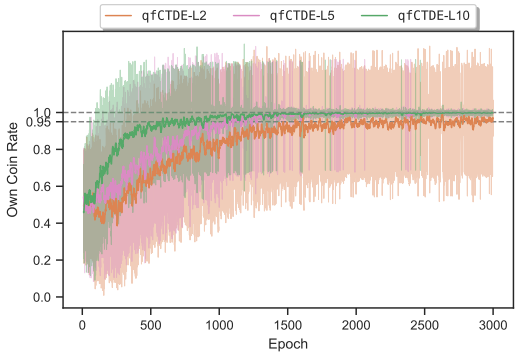

(f) qfCTDE - POMDP - Own Own Coin Rate

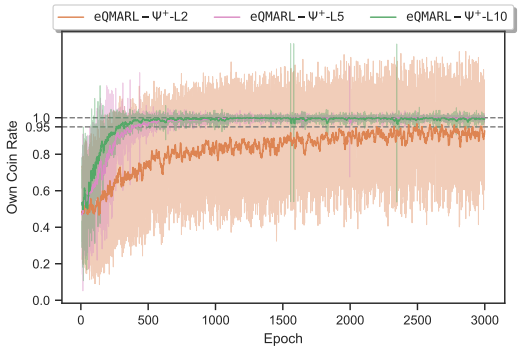

(g) eQMARL-Ψ^+ - MDP - Own Own Coin Rate

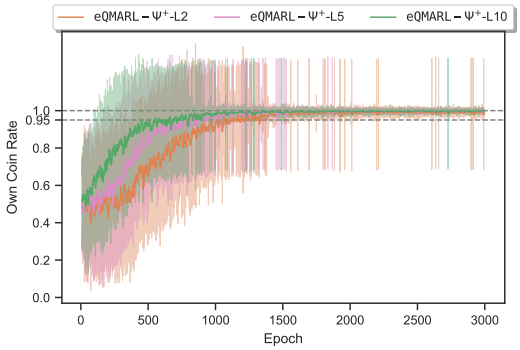

(h) eQMARL-Ψ^+ - POMDP - Own Own Coin Rate

Figure H.5: Own Coin Rate performance for ablation study using `CoinGame-2` for (a,b) fCTDE, and (c,d) sCTDE, and (e,f) qfCTDE, and (g,h) eQMARL-Ψ^+ with hidden layer units $h \in \{3, 6, 12, 24\}$ and VQC layers $L \in \{2, 5, 10\}$, averaged over 10 runs of 3000 epochs, with ± 1 std. dev. shown as shaded regions.